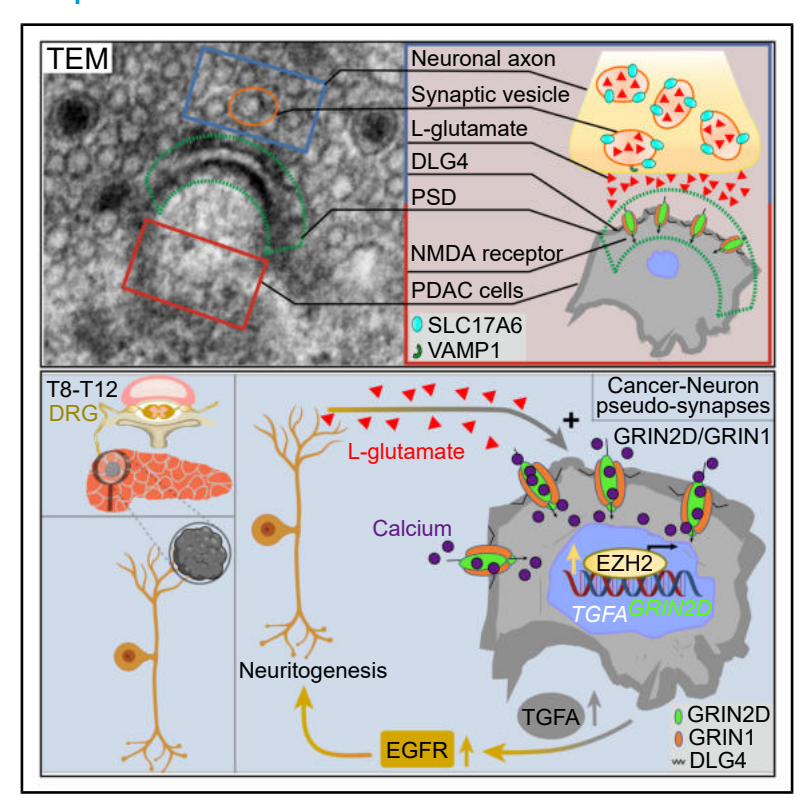
Cancer Cell

Sensory neurons drive pancreatic cancer progression through glutamatergic neuron-cancer pseudo-synapses

Graphical abstract



Authors

Lei Ren, Chunfeng Liu, Kaan Çifcibaşı, ..., Güralp O. Ceyhan, Rouzanna Istvanffy, Ihsan Ekin Demir

Correspondence

ekin.demir@tum.de

In brief

Ren et al. demonstrate pseudo-synaptic connections between sensory neurons and pancreatic ductal adenocarcinoma (PDAC) cells. These pseudo-synapses exhibit enrichment of NMDA receptor subunit GRIN2D/GluN2D, enhancing PDAC responsiveness to neuron-derived glutamate and promoting tumor growth. Disrupting glutamate-GRIN2D signaling at pseudo-synapses improves survival in PDAC, highlighting the therapeutic potential of targeting cancer-neuron-pseudo-synapses.

Highlights

- Demonstration of cancer-sensory-neuron-pseudo-synapses in an extracerebral cancer
- PDAC cells enrich the NMDAR subunit GRIN2D at cancerneuron pseudo-synaptic sites
- Glutamate drives PDAC progression through GRIN2D signaling at pseudo-synapses
- Disrupting GRIN2D signaling enhances survival in pancreatic cancer models



Cancer Cell



Article

Sensory neurons drive pancreatic cancer progression through glutamatergic neuron-cancer pseudo-synapses

Lei Ren, 1,2,4,5 Chunfeng Liu, 3 Kaan Çifcibaşı, 1 Markus Ballmann, 6 Gerhard Rammes, 6 Carmen Mota Reyes, 1,4,5,19 Sergey Tokalov, 1,4,5 Andreas Klingl, 7 Jennifer Grünert, 7 Keshav Goyal, 7 Peter H. Neckel, 8 Ulrich Mattheus, 8 Benjamin Schoeps, 9 Saliha Elif Yıldızhan, 10 Osman Ugur Sezerman, 10 Nedim Can Cevik, 11 Elif Arik Sever, 11 Didem Karakas, 11 Okan Safak, 1 Katja Steiger, 5,12 Alexander Muckenhuber, 5,12 Kıvanç Görgülü, 4,5,13 Zongyao Chen, 1 JingCheng Zhang, 1 Linhan Ye, 1 Mohammed Inayatullah Maula Ali, 14 Vijay K. Tiwari, 14 Nataliya Romanyuk, 15 Florian Giesert, 16 Dieter Saur, 4,5,17 Roland Rad, 4,5,18 Roland M. Schmid, 19 Hana Algül, 4,5,13 Achim Krüger, 9 Helmut Friess, 1,4,5,13 Güralp O. Ceyhan, 11,20 Rouzanna Istvanffy, 1,4,5,20,22 and Ihsan Ekin Demir, 4,5,11,20,21,22,23,*

SUMMARY

Cancers thrive on neuronal input. Here, we demonstrate the presence of pseudo-synaptic connections between sensory nerve endings and cancer cells in an extracerebral cancer, i.e., pancreatic ductal adenocarcinoma (PDAC). These synaptic sites exhibit a selective enrichment of the glutamatergic N-methyl-D-aspartate receptor (NMDA) receptor subunit NMDAR2D (GRIN2D) on the cancer cells, which turns PDAC cells responsive to neuron-derived glutamate and promotes tumor growth and spread. Intriguingly, neurons transform a subset of co-cultured PDAC cells into calcium-responsive cells via GRIN2D-type glutamate receptors at the neuron-cancer pseudo-synapses. We found that the expression of this subunit is due to the increased glutamate availability provided by sensory innervation in a neurotrophic feedforward loop. Moreover, interference with the glutamate-GRIN2D signaling at these neuron-cancer pseudo-synapses markedly improved survival *in vivo*. This discovery of peripheral cancer-neuron pseudo-synapses may provide an opportunity for cancer-neuroscience-instructed oncological therapies.

¹Department of Surgery, Klinikum rechts der Isar, Technical University of Munich, School of Medicine, Munich, Germany

²Department of General Surgery (Gastrointestinal Surgery), the Affiliated Hospital of Southwest Medical University, Luzhou 646000, China

³Department of Respiratory and Critical Care Medicine, the Affiliated Hospital of Southwest Medical University, Luzhou 646000, China

⁴German Cancer Consortium (DKTK), Partner Site Munich, Germany

⁵CRC 1321 Modelling and Targeting Pancreatic Cancer

⁶Department of Anesthesiology and Intensive Care, Klinikum rechts der Isar, Technical University Munich, School of Medicine, Munich, Germany

⁷Plant Development, Biocenter LMU Munich, Ludwig Maximilians Universität, Munich, Germany

⁸Institute of Clinical Anatomy and Cell Analysis, University of Tübingen, Tübingen, Germany

⁹Institute of Experimental Oncology and Therapy Research, Technical University of Munich, School of Medicine, Munich, Germany

¹⁰Department of Bioinformatics and Medical Informatics, Acibadem Mehmet Ali Aydinlar University, Istanbul, Turkey

¹¹Department of General Surgery, HPB-Unit, School of Medicine, Acibadem Mehmet Ali Aydinlar University, Istanbul, Turkey

¹²Comparative Experimental Pathology and Institute of Pathology, Technical University of Munich, School of Medicine, Munich, Germany

¹³Comprehensive Cancer Center Munich, Klinikum rechts der Isar, Technical University of Munich, School of Medicine, Munich, Germany

¹⁴Institute for Molecular Medicine, University of Southern Denmark, Campusvej 55, 5230, Odense M, Denmark

¹⁵Department of Neuroregeneration, Institute of Experimental Medicine, CAS, Vestec, Czechia

¹⁶Institute of Developmental Genetics, Helmholtz Munich, Oberschleissheim, Germany

¹⁷Institute of Translational Cancer Research (TranslaTUM) and Experimental Cancer Therapy, Technical University of Munich, School of Medicine, Munich, Germany

¹⁸Institute of Molecular Oncology and Functional Genomics, Technical University of Munich, School of Medicine, Munich, Germany

¹⁹Department of Internal Medicine II, Klinikum rechts der Isar, Technical University of Munich, School of Medicine, Munich, Germany

²⁰Neural Influences in Cancer (NIC) International Research Consortium, Munich, Germany

²¹Else Kröner Clinician Scientist Professor for Translational Pancreatic Surgery, Munich, Germany

²²These authors contributed equally

²³Lead contact

^{*}Correspondence: ekin.demir@tum.de https://doi.org/10.1016/j.ccell.2025.09.003



INTRODUCTION

Pancreatic ductal adenocarcinoma (PDAC) is a highly lethal malignancy, ranking among the primary contributors to tumor-associated mortality worldwide. 1-7 Human PDAC demonstrates an exceptionally high incidence of neural invasion (NI) and neuroplastic alterations.8-11 Cancer cells infiltrating nerves exploit them as conduits for dissemination, resulting in extensive local invasion, rendering surgical intervention infeasible, and inducing severe pain. 8,11-15 The severity of NI in PDAC serves as an independent prognostic factor of overall and disease-free survival, as well as local recurrence. 16-18 In line with the prognostic significance of NI, both sensory and sympathetic peripheral nerves have been shown to promote tumorigenesis and tumor aggressiveness in murine PDAC. 19-23 Notably, while the mechanisms underlying sensory nerve-pancreatic cancer interactions in the murine PDAC have been partly elucidated, their scope has been primarily limited to paracrine signaling pathways.²⁴

Both primary and metastatic tumors of the central nervous system have been previously shown to thrive under synaptic glutamate signaling between central nervous system neurons and cancer cells. ^{26–29} Although L-glutamate serves as a predominant neurotransmitter of peripheral dorsal root ganglion (DRG) sensory neurons, ³⁰ the existence of glutamate-mediated, synaptic interactions between sensory neurons and peripheral cancer cells, such as PDAC cells, remains unexplored. Thus, driven by the prognostic significance of NI in PDAC and the critical role of synaptic glutamate signaling in central nervous system cancers, we investigated the potential presence of similar, previously unexplored synaptic glutamate signaling interactions between peripheral sensory neurons and extracerebral cancer cells.

RESULTS

GRIN2D is upregulated in various human cancers and promotes cancer cell migration

To dissect the involvement of glutamate signaling in PDAC, we initially analyzed the expression of individual glutamate receptor subtypes within patient-derived PDAC tumor biopsies and corresponding human celiac ganglia specimens obtained from our biobank. Subsequently, we extended our analysis to include human PDAC tissues derived from The Cancer Genome Atlas Program (TCGA) database. Notably, we observed a marked elevation in the expression levels of the GRIN2D gene, a member of the NMDAR family of glutamate receptors, among all glutamate receptors analyzed, prompting our focus on NMDAR components (Figures 1A and 1B). Elevated expression levels of GRIN1, GRIN2A, and GRIN2D were identified in PDAC compared to normal human pancreas (Figure S1A). Interestingly, among the overexpressed genes, only GRIN2D exhibited a significant association with the T and N stages of the TNM status (Figures S1B and S1C), which implies GRIN2D expression levels may correlate with tumor progression and the extent of lymph node invasion. The broader significance of GRIN2D in cancer was underscored by its elevated expression across multiple human cancers when compared to normal tissue (Figure S1D). Utilizing an analysis based on the heterotetrameric assembly of NMDARs, our investigation revealed a notable co-expression pattern and a particularly significant correlation exclusively between GRIN1 and GRIN2D genes, among the NMDAR components, within human PDAC samples (Figure S1E). Strikingly, expression levels of all glutamatergic receptors and their subunits in previously characterized human neuro-affine SU.86.86 and T3M4 and non-neuro-affine Panc-1 and Capan-1 cell lines³¹ were consistent with our TCGA-based analyses, with GRIN2D exhibiting the highest expression among the NMDAR subtypes, accompanied by coexpression of GRIN1 (Figures S1F-S1I). Similar results were observed in our non-neuro-affine murine KPC and neuro-affine TPAC cell lines, ²⁵ with *Grin2d* being expressed the highest among all glutamate receptor genes (Figures S1J and S1K). These findings imply an enhanced cellular responsiveness to glutamate signaling, consistent with previous literature demonstrating that the NR1 (GRIN1, encoded by GRIN1) and NR2 (GRIN2) subunits form receptor complexes characterized by heightened sensitivity to glutamate, NMDA, glycine, and D-serine. 32

To investigate the cellular specificity and functional relevance of *GRIN2D* in PDAC, we analyzed two single-cell RNA sequencing (scRNA-seq) datasets (325,480 cells from 70 human PDAC tumors). ^{33,34} *GRIN2D* was selectively enriched in malignant epithelial cells, with minimal expression in non-malignant populations (Figures 1C, 1D, and S2A-S2D). Further analysis of treatment-naive and FOLFIRINOX-treated tumors revealed higher *GRIN2D* expression in untreated tumors compared to those with minimal, moderate, or poor treatment responses (Figure S2E). ³³ These data highlight a tumor-cell-intrinsic role for *GRIN2D* and nominate it for functional and therapeutic investigation.

To assess the impact of L-glutamate (L-Glu), a ligand of the GRIN2D subunit encoded by the GRIN2D gene, we evaluated the migratory abilities of neuro-affine cell lines SU.86.86. T3M4, and TPAC and compared them with the non-neuro-affine cancer cell lines Panc-1, Capan-1, and KPC. 25,31 Here, we tested various L-Glu concentrations on cancer cells and found that 0.5 µM of L-Glu optimally stimulated the GRIN2D transcription in cancer cells, while cell growth remained unchanged (Figures S2F-S2L). Interestingly, neuro-affine cell lines SU.86.86, T3M4, and TPAC showed increased migration and invasion when treated with L-Glu and DRG-conditioned media (CM), whereas non-neuro-affine cells Panc-1, Capan-1, and KPC did not (Figures 1E-1G). Furthermore, pretreatment with a selective antagonist for GRIN2D, i.e., UBP145, effectively reversed the migratory and invasive behaviors of SU.86.86, T3M4, and TPAC cells, but not in non-neuro-affine cell lines (Figures 1H, 1I, and S2M). GRIN2D siRNA silencing in SU.86.86 and Capan-1 cells mirrored UBP145 inhibitory effects on migration and invasion triggered by L-Glu or DRG CM, especially in neuro-affine SU.86.86 cells (Figures 1J-1L).

Collectively, these results showed that L-Glu enhances the migratory phenotype of neuro-affine PDAC cells, mediated by the NMDAR receptor subtype GRIN2D.

GRIN2D expression in cancer cells correlates with an increased abundance of presynaptic glutamate-release-associated proteins in neurons

In further analyses, we explored the correlation between GRIN2D, GRIN1, and proteins linked to presynaptic vesicular glutamate transport, including vesicle-associated membrane protein 1 (*VAMP1*)³⁵ and solute carrier family 17 member 6



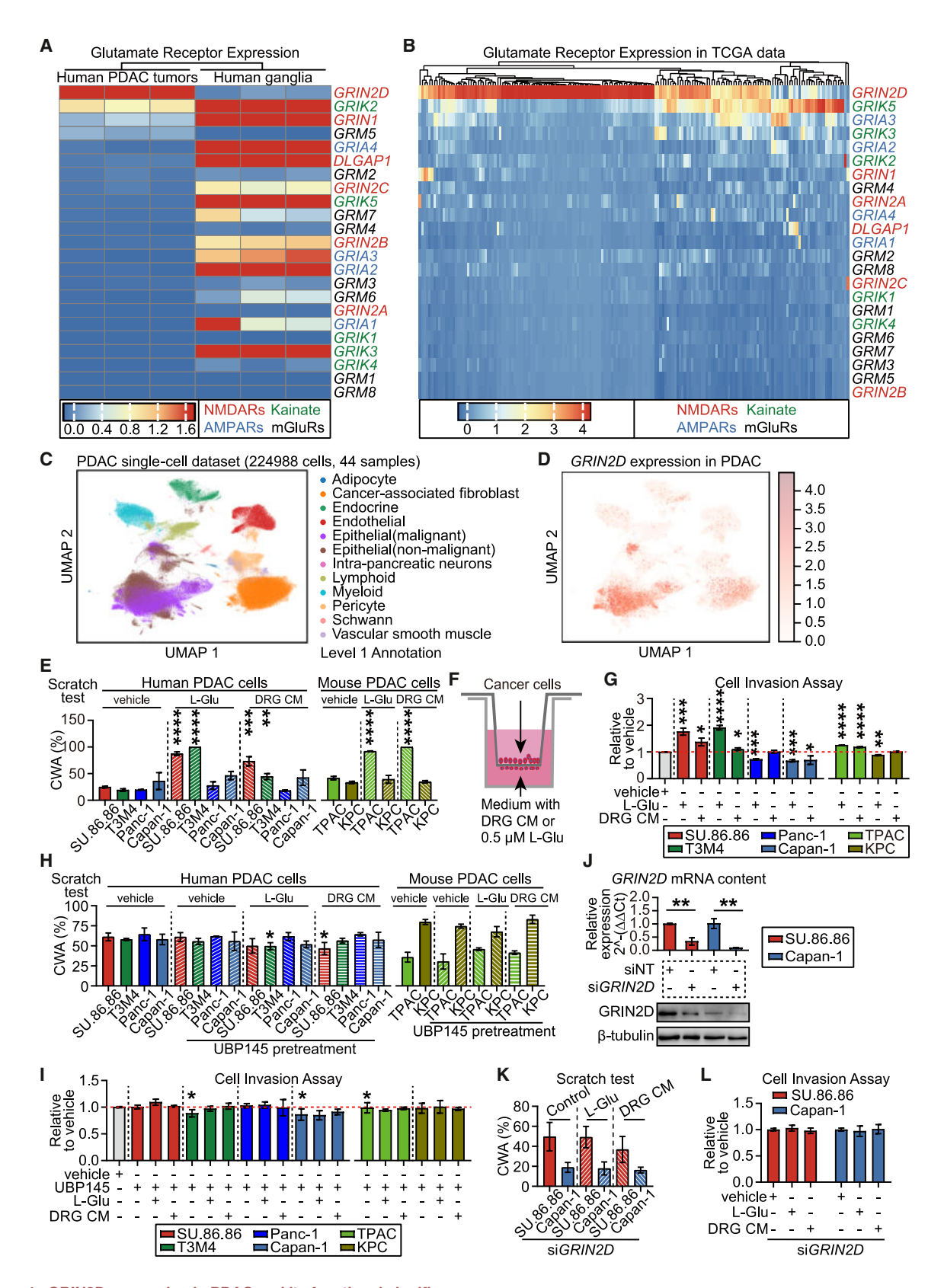


Figure 1. GRIN2D expression in PDAC and its functional significance

(A) Expression of 23 glutamate-receptor-associated genes in human PDAC and matched celiac ganglia. Color scale: blue (low expression) to red (high expression), with a value range of 0.0–1.6; gene labels are colored by receptor type: NMDARs (brick red), AMPARs (steel blue), Kainate (dark green), and mGluRs (black).



(SLC17A6),36 as well as the postsynaptic density protein 95 (PSD95/DLG4, encoded by DLG4).37,38 Looking first at the cancer cells, our investigation audited the levels of the nine glutamate transporter genes using RT-qPCR across human SU.86.86 and Capan-1, as well as murine TPAC and KPC cells. Expression levels were largely comparable and low across cell types, with the exception of SLC1A3 and Slc7a11, which were respectively elevated in human and murine cell lines (Figures S3A and S3B). However, western blot analyses revealed that SLC1A3 and SLC7A11, two transporter proteins capable of exporting glutamate, were present in insignificant amounts in the compared cell lines, with a similar result on SLC17A6 (encoded by SLC17A6), a key vesicular protein for glutamate loading into synaptic vesicles (Figure S3C). Hence, the expression levels of the glutamate transporter genes in the cancer cells were not in relevant amounts.

Subsequently, we unveiled the co-expression of GRIN2D and GRIN1 in human PDAC tissue and synchronously elevated levels compared to normal pancreatic tissue (Figures S3D and S3E), then further uncovered a significant enrichment of GRIN2D and GRIN1 proteins, as well as DLG4, within cancer cells invading nerves, in contrast to cancer cells not involved in neural invasion (Figure 2A). Furthermore, notably elevated levels of VAMP1 (synaptobrevin-1, encoded by VAMP1) and SLC17A6 (vesicular glutamate transporter 2, vGlut-2) were observed in nerves invaded by cancer cells compared to non-invaded nerves (Figure 2B). Moreover, exposure to DRG CM resulted in the upregulation of GRIN1 (Grin1) and GRIN2D (Grin2d) in neuro-affine SU.86.86, T3M4, and TPAC cells, differing from their non-neuroaffine counterparts, with Capan-1 cells displaying a significant decrease in GRIN1 and GRIN2D mRNA expressionFigures S3. Notably, treatment with DRG CM significantly augmented the protein expression of GRIN2D, GRIN1, and DLG4 in human neuro-affine cancer cell lines, particularly in SU.86.86 cells. Conversely, non-neuro-affine Panc-1 and Capan-1 cells showed unaltered or decreased levels of the analyzed proteins following DRG CM treatment (Figures S3F-S3H). Furthermore, prominent expression of GRIN2D, GRIN1, and DLG4 in cancer cells and VAMP1 and SLC17A6 in neurons was detectable via immunocytochemistry in SU.86.86-DRG co-cultures. Conversely, the respective expressions were notably less prominent in Capan-1-DRG co-cultures (Figures 2C and 2D). Consistently, coculturing with DRGs elevated the protein expression of GRIN1, GRIN2D, and DLG4 in neuro-affine SU.86.86 and T3M4 cells but not in non-neuro-affine Panc-1 and Capan-1 cells (Figures S3I and S3J). Interestingly, depletion of the GRIN2D gene reversed this effect in SU.86.86 cells and affected the induction of GRIN1 and DLG4 expression, which was not observed in Capan-1 cells (Figure S3K). Altogether, these data suggest that cancer cell expression of specific NMDAR subunits, particularly of GRIN2D, is accompanied by the neuronal expression of presynaptic glutamate transport proteins.

Glutamate triggers GRIN2D expression via the CAMK IV-**CREB** pathway and **E2F1-mediated** activation of **EZH2**

Utilizing data from the ARCHS4 database, we identified enhancer of Zeste 2 polycomb repressive complex 2 subunit (EZH2) as the most potentially significant transcription factor (TF) governing GRIN2D expression in human cells. Initially, in the TCGA dataset, among NMDAR subunits, only GRIN1 and GRIN2D showed co-expression and a positive correlation with EZH2 expression in human PDAC cells (Figures S4A and S4B). To corroborate these findings, we conducted a chromatin immunoprecipitation PCR assay (ChIP-PCR). The results identified two potential binding sites for EZH2 within the region of the GRIN2D gene (Figure S4C). Furthermore, we observed an increase in the enrichment of EZH2 binding to the GRIN2D upon treatment of SU.86.86 cells with L-Glu (Figure 3A). Remarkably, synchronized elevations in GRIN2D and EZH2 levels were exclusively detected in neuro-affine human PDAC cells subsequent to L-Glu treatment. Conversely, no comparable effect was observed in non-neuro-affine PDAC cells (Figure S4D). Immunocytochemistry analyses further revealed that both L-Glu and DRG CM upregulated EZH2 levels in SU.86.86 cells but not in Capan-1 cells (Figure 3B). Furthermore, GRIN2D levels were notably decreased in EZH2 siRNA-silenced group following treatment with L-Glu and DRG CM (Figures 3C and 3D).

The E2F transcription factor 1 (E2F1), a well-known key transcription factor for EZH2 expression, has been shown to uprequlate EZH2 levels in a dose-dependent manner. 39 Consistent with this, we observed that silencing of E2F1 significantly reduced E2F1 enrichment at the EZH2 promoter in SU.86.86 cells, as evidenced by ChIP-PCR analysis (Figure 3E). We identified three corresponding E2F1 binding sites located at the EZH2 promoter (Figure S4E). Subsequently, EZH2 expression was notably downregulated following siRNA-mediated silencing of E2F1 in SU.86.86 cells (Figure 3F). Next, we scrutinized the hypothesized EZH2-E2F1 signaling pathway as the putative regulatory mechanism upstream of GRIN2D. EZH2 exerts its function as a transcription repressor by catalyzing the trimethylation of histone 3 lysine 27 (H3K27me3), thereby facilitating cell proliferation through the suppression of cyclin-dependent kinase (CDK) inhibitors, particularly p16^{INK4a} (encoded by CDKN2A; hereafter CDKN2A). 40,41 CDKN2A was shown to negatively regulate CDK4, which is a key oncogenic driver and regulator within the CDK family.⁴² CDK4 forms a complex with its regulatory cyclin

⁽B) Expression of 23 glutamate-receptor-associated genes in 177 PDAC patients from TCGA, ranked by glutamatergic Z scores. Color scales (range 0-4) and gene label colors are the same as in (A).

⁽C and D) UMAP of 224,988 cells from 44 PDAC samples (GSE202051)³³; (C) depicts cell type diversity; (D) visualizes GRIN2D expression (dark red: high; light orange: low).

⁽E) Closed wound area (CWA) after treatment with L-glutamate (L-Glu) or dorsal root ganglion conditioned medium (DRG CM).

⁽F) Schematic illustration of cancer cell invasion.

⁽G) Quantification of cancer cell invasion following the same treatments.

⁽H-L) CWA and invasion in PDAC cells pretreated with UBP145 (H-I) or GRIN2D siRNA (siGRIN2D; J-L), followed by L-Glu or DRG CM; knockdown efficiency of siGRIN2D and non-targeting siRNA (siNT) shown.

All data are mean \pm SEM, n = 3. Unpaired t test; *p < 0.05, **p < 0.01, ****p < 0.001, ****p < 0.0001. Also see Figures S1 and S2.



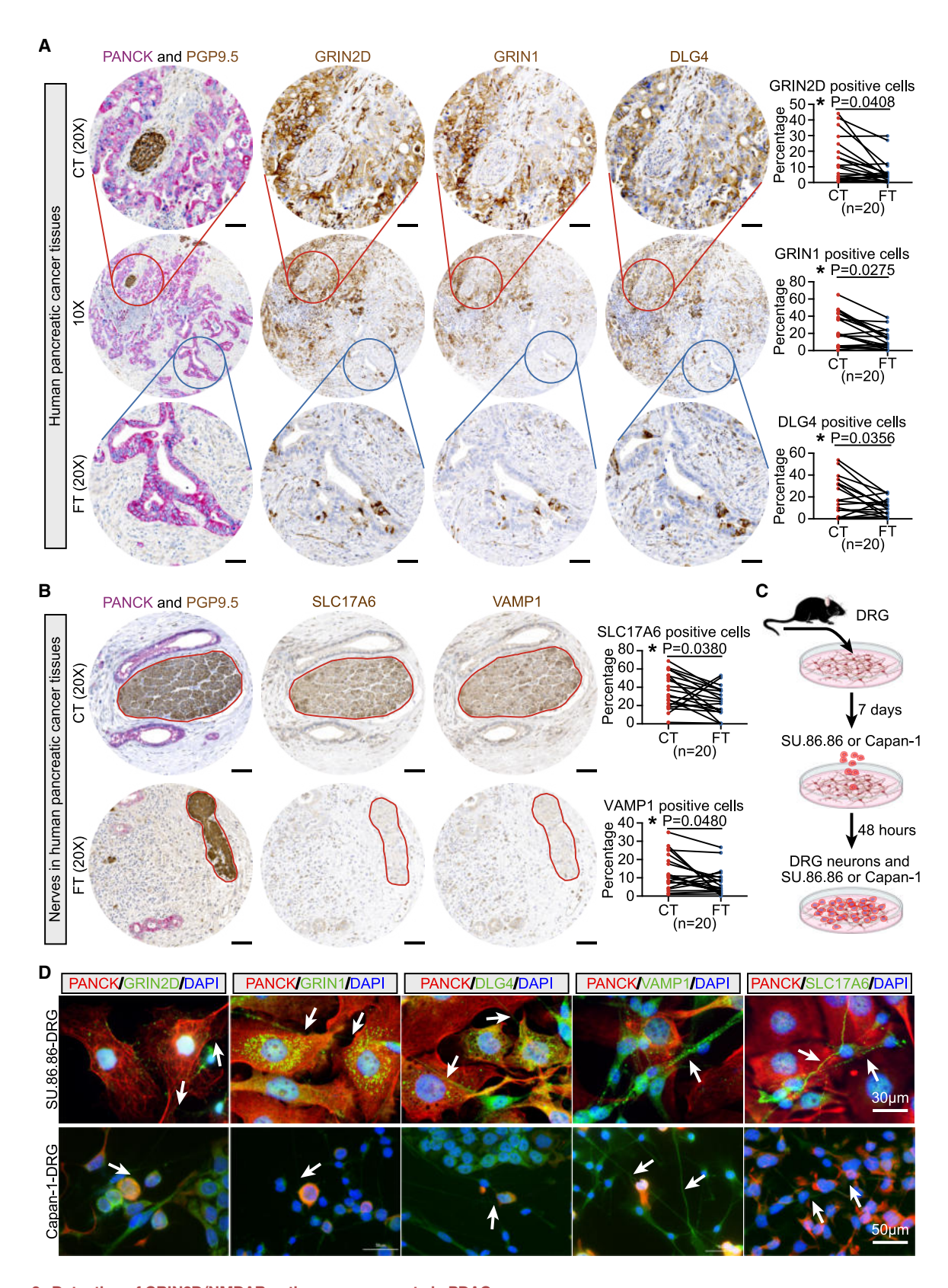


Figure 2. Detection of GRIN2D/NMDAR pathway components in PDAC

(A) Immunostaining of PANCK, PGP9.5, GRIN2D, GRIN1, and DLG4 in 20 human PDAC specimens. CT, nerves close to tumors (with neural invasion); FT, nerves farther from tumors (without neural invasion). Scale bars, 20 μm.



subunit, cyclin D1 (encoded by *CCND1*). Upon activation, the CDK4-CCND1 complex phosphorylates and inactivates the tumor suppressor protein RB, leading to the liberation of E2F1.⁴³

Our experiments revealed significant alterations in the EZH2-E2F1 axis signaling molecules in SU.86.86 cells upon treatment with L-Glu or DRG CM. Specifically, EZH2, H3K27me3, pRB^{Ser780}, E2F1, CyclinD1, and CDK4 protein levels were elevated, while CDKN2A expression was decreased. Conversely, Capan-1 cells did not exhibit any difference in the expression of these proteins (Figures 3G and S4F-S4H). Furthermore, L-Glu treatment notably increased EZH2 and H3K27me3 levels, while decreasing CDKN2A expression in SU.86.86 cells. However, transfection with EZH2 siRNA reversed the changes in the expression of CDK2NA and H3K27me3 (Figure S4I). Additionally, the downregulation of EZH2 via siRNA led to a decrease of E2F1 and pRB^{Ser780} in SU.86.86 cells treated with L-Glu and DRG CM (Figure S4J). These findings highlight the pivotal role of the EZH2-E2F1-p-Rb signaling pathway as the upstream regulatory mechanism driving GRIN2D expression in PDAC.

It is known that the physiological impact of glutamate, particularly ligand-stimulated NMDAR activation, triggers calcium influx in neurons, thereby instigating the downstream calcium-/ calmodulin-dependent protein kinase 4 (CAMK4) pathway. 26,44 On the other hand, EZH2 expression is positively regulated by the transcription factor cyclic AMP-responsive element-binding protein 1 (CREB1) phosphorylated at Ser133.^{26,45–47} Therefore, we investigated whether a similar glutamate-triggered activation of the CAMK4-EZH2 pathway occurs in our neuro-affine cancer cells. Our results revealed a synchronous activation of CAMK4 and pCREB1^{Ser133} in SU.86.86 cells following L-Glu treatment (Figure S4K). Importantly, these changes were abrogated upon CAMK4 silencing, leading to a glutamate-dependent decrease in EZH2 level (Figures 3H and S4L). Thus, our data further support the involvement of glutamate in the upstream regulatory mechanism of GRIN2D expression through the activation of the CAMK4-CREB1 signaling pathway.

Next, we investigated the functionality of the GRIN2D-containing glutamatergic receptors on cancer cells. Using calcium imaging recordings in neuron-cancer cell co-cultures, we confirmed the presence of functional GRIN2D-containing NMDA receptors in human SU.86.86 cells, as evidenced by glutamate-induced responses in cells co-cultured with human neurons differentiated from the human neural progenitor cell line SPCs-01. The glutamate-evoked calcium influx was dosedependent and modulated by specific NMDA receptor antagonists, such as UBP141 and AP5, which further support the functional role of GRIN2D in SU.86.86 cells, with a resting membrane potential of -50.07 ± 3.33 mV in pancreatic cancer cells (Figures 3I-3L and S4M). Importantly, no response was observed on mono-cultured SU.86.86 cells (Figure 3M), which suggests the necessity of the physical proximity/contact of neurons to cancer cells for the operational GRIN2D signaling in pancreatic cancer cells. Moreover, our findings indicated that SU.86.86 exhibited spontaneous calcium influx in the absence of external stimulation but in co-culture with neurons. This activity appears to be primarily dependent not on L-Glu, but more on L- and T-type calcium channels, which suggests GRIN2D likely functions as a glutamate "sensor," and calcium influx into the cancer cell at the pseudo-synapse is presumably induced by activation of sensory neurons (Figure S4N). Moreover, we also confirmed that exogenously applied NMDA activated Ca²⁺ currents specifically on cancer cells, indicating the functionality of GRIN2D-mediated signaling in SU.86.86 cells co-cultured with murine DRG neurons, a response not observed in SU.86.86 mono-cultures (Figures S4O and S4P).

Grin2d in murine pancreatic cancer cells is essential for tumor growth and innervation

To elucidate the biological significance of *Grin2d* in cancer cells, we utilized two distinct approaches: knockdown of the Grin2d with short hairpin RNA (shRNA) (shGrin2d) and knockout (KO) of the *Grin2d* gene with the CRISPR-Cas9 system (*Grin2d*^{-/-}). The editing was performed in a commercially available KPC-Pdx1CRE cell line characterized by high repopulation rates. These cells express Cre recombinase under the control of the Pdx1 promoter and harbor a conditionally expressed Trp53^{R175H} mutant allele, similar to the Li-Fraumeni human ortholog TP53^{R175H}.⁴⁸ Notably, our primary KPC line features a p48-Cre cassette, which replaces exons one and two of the Ptf1a gene, and conditional KO of Trp53 gene. 49,50 The expression level of Grin2d in KPC-Pdx1CRE cells is comparable to that of TPAC, and both are higher than those in primary KPC cells, while immunofluorescence staining showed elevated baseline GRIN2D levels in tumors from KPC-Pdx1CRE-implanted mice compared to those from KPC mice (Figures S5A and S5B). The editing efficiency of the generated shGrin2d cells was verified with RTqPCR and western blotting, revealing a significant reduction in Grin2d at both mRNA and protein levels (Figure 4A). In Grin2d KO cells, targeting the critical exon three of the Grin2d gene with intronic gRNAs resulted in complete protein depletion (Figure 4B).

The functional characterization unveiled a lack of response in both shGrin2d and $Grin2d^{-/-}$ cells to treatment with L-Glu and DRG CM, as determined through invasion, migration, and wound healing assays (Figures S5C–S5G). Moreover, no differences were observed in cell metabolic activity, as assessed by the MTT assay, nor in colony formation properties (Figures S5H–S5K).

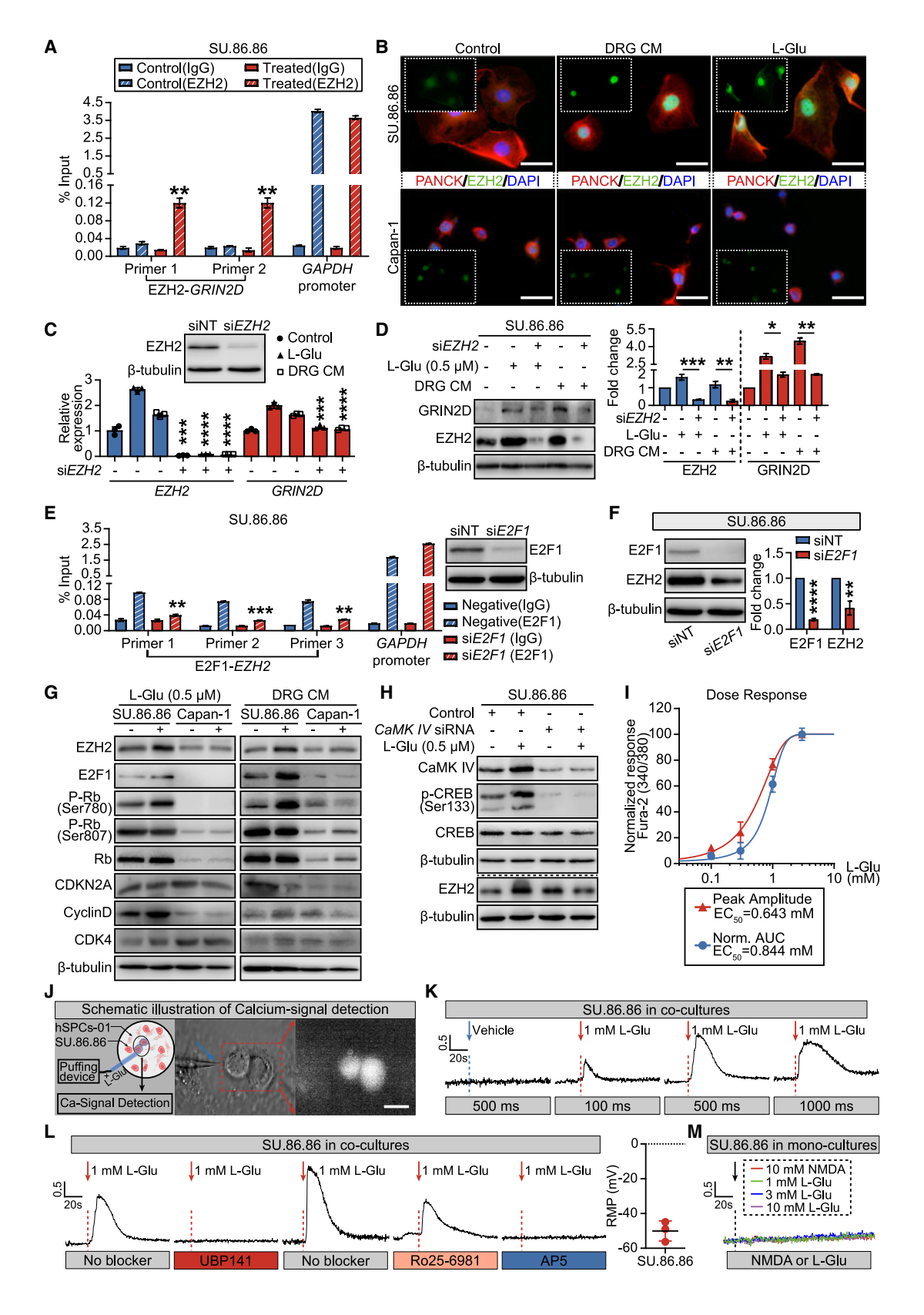
To validate the impact of *Grin2d* depletion *in vivo*, we implanted KPC-Pdx1CRE *Grin2d*^{-/-} and sh*Grin2d* cells, along with corresponding control cells (*Grin2d*^{+/+} and shNT with unmodified *Grin2d* gene), orthotopically into the pancreas of six-week-old female C57BL/6N mice, as previously described⁵¹ (Figure 4C). The overall survival of mice implanted with sh*Grin2d* and *Grin2d*^{-/-} cell groups was significantly increased compared to their respective controls (Figure 4D).

⁽B) SLC17A6 and VAMP1 staining in the same specimens. "CT"/"FT" as in (A). Scale bars, 20 μm .

⁽C) Schematic of cancer-neuron co-cultures for immunocytochemistry.

⁽D) Immunostaining of PANCK, GRIN1, GRIN2D, DLG4, SLC17A6, and VAMP1 in SU.86.86-dorsal root ganglion (DRG) and Capan-1-DRG co-cultures. White arrowheads: axons. All data are mean ± SEM. Unpaired t test; *p < 0.05. Also see Figure S3.





(legend on next page)



The prolonged survival corresponded to a reduced tumor growth rate in the shGrin2d and $Grin2d^{-/-}$ groups compared to their controls, monitored over 55 days post-implantation. Furthermore, a significant reduction in tumor volume was observed upon reaching the experimental endpoint, resulting in decreased pancreas weight, accompanied by a reduction in the number of peritoneal metastases (Figures 4E and S6A-S6F). Moreover, both shGrin2d and Grin2d^{-/-} groups showed reduced glutamate levels in the pancreas, but increased levels in the pancreas-innervating DRGs T8-T12, while serum glutamate levels remained unchanged (Figures 4F, 4G, S6G, and S6H). The reduced tumor size could also be explained by elevated cleaved caspase 9 levels in Grin2d-/- and shGrin2d tumors (Figures 4H and S6I). Furthermore, the shGrin2d and Grin2d^{-/-} groups demonstrated diminished innervation of the tumors and surrounding tissue, as evidenced by decreased levels of PGP9.5, a prominent marker of peripheral neurons, compared to their respective control groups (Figures 4I and S6J). Additionally, the protein expression of GRIN2D was diminished in both the shGrin2d and Grin2d^{-/-} groups, concomitant with the downregulation of transcription factors EZH2 and CaMK4, known regulators upstream of Grin2d gene expression (Figures 4I and S6J).

Collectively, these data suggest that the expression of *Grin2d* in cancer cells plays a pivotal role in tumor progression and innervation *in vivo*. This may potentially trigger glutamate overproduction in sensory dorsal root ganglia neurons, thereby initiating a positive feedback loop between cancer cells and sensory neurons, driving tumor growth *in vivo*.

Sensory innervation drives the *Grin2d* upregulation in pancreatic cancer cells in a feedforward loop via TGFA-EGFR signaling

To unravel the potential molecular mechanisms driving *Grin2d*-mediated tumor innervation, we conducted mRNA sequencing of orthotopically implanted *Grin2d*^{-/-} and *Grin2d*^{+/+} tumors. Among the candidates, seven neurotrophic factors or receptors, including *Fgf1*, *Fgfr4*, *Egfr*, *Gmfg*, *Tgfb1i1*, *Efnb1*, *and Tgfa*, stood out as potential mediators of innervation (Figures 5A and S7A). Subsequent validations through RT-qPCR revealed *Egfr*

and its ligand transforming growth factor α (TGFA) as focal points of interest, given their significant downregulation in the $Grin2d^{-/-}$ implanted tumors (Figure 5B). Remarkably, similar trends were evident in EGFR protein levels in Grin2d-edited KPC-Pdx1CRE cells (Figure S7B). To delve deeper, we explored the impact of TGFA on DRG neurons in vitro and demonstrated EGFR activation in murine DRG neurons post-recombinant TGFA treatment (Figure 5C). This treatment corresponded with increased axonogenesis (Figures 5D and S7C). Additionally, immunohistochemistry staining validated the reduced levels of EGFR and its ligand TGFA in $Grin2d^{-/-}$ and Srin2d orthotopically implanted tumors (Figures 5E and S7D). In summary, our investigations delineated the role of GRIN2D-triggered EGFR-TGFA signaling in fostering peritumoral innervation in PDAC.

We then explored whether it is sensory nerves and L-glutamate of sensory nerves that drive Grin2d expression in cancer cells. Here, we employed capsaicin-mediated ablation of TRPV1+ DRG neurons in vitro. We observed that the increase in the number of DRG neurons corresponded to elevated TRPV1 expression within KPC-Pdx1CRE cell-neuron co-cultures (Figure S7E). Subsequent co-cultures of KPC-Pdx1CRE cells with DRGs pretreated with capsaicin revealed decreased TRPV1 expression, as indicated by immunocytochemistry staining (Figures 5F, S7F, and S7G). Consistent results were obtained through ELISA measurements of TRPV1, substance P (SP), and CGRP in cell lysates and/or supernatants from co-cultures of KPC-Pdx1CRE cells with different numbers of DRGs, showing decreased expression resembling capsaicin treatment in KPC-Pdx1CRE-neuron co-cultures, even when Grin2d was deleted in KPC-Pdx1CRE cells (Figures 5G-5I and S7H). Additionally, capsaicin-treated KPC-Pdx1CRE-DRG co-cultures exhibited reduced GRIN2D content, which was reversible with L-Glu treatment (Figure 5J). Overall, our data suggest that sensory neurons regulate cancer cell GRIN2D expression in a glutamate-dependent manner.

To validate this observation *in vivo*, we implanted KPC-Pdx1CRE- $Grin2d^{-/-}$ and corresponding control cells (KPC-Pdx1CRE- $Grin2d^{+/+}$) into the pancreas of 42-day-old C57BL/6N mice (both sexes) that were treated with capsaicin

Figure 3. EZH2-mediated GRIN2D expression in PDAC cells in response to L-glutamate

(A) ChIP-PCR showing EZH2 binding to GRIN2D in SU.86.86 cells after L-glutamate (L-Glu) treatment.

(B) Immunostaining of EZH2 in SU.86.86 and Capan-1 cells following dorsal root ganglion conditioned medium (DRG CM) or L-Glu treatment. White boxes indicate single-channel EZH2 staining to highlight signal intensity. Scale bars, 50 μm.

(C and D) Validation of EZH2 siRNA (siEZH2) and non-targeting siRNA (siNT) efficacy and analysis of GRIN2D and EZH2 expression in siEZH2-pretreated SU.86.86 cells after L-Glu and DRG CM treatment by RT-PCR (C) and western blot (D).

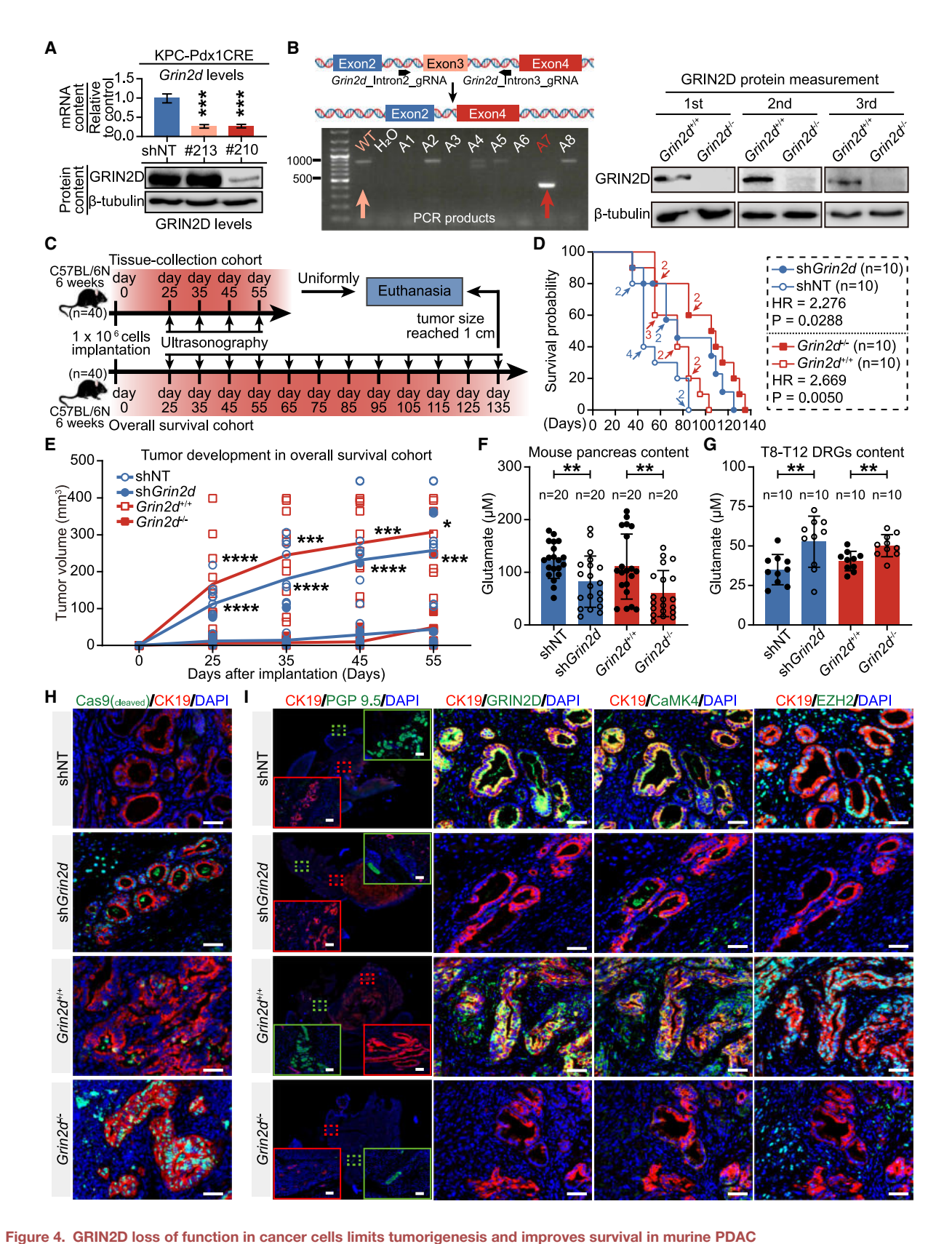
- (E) E2F1 binding to EZH2 promoter by ChIP-PCR. Western blot showing E2F1 siRNA (siE2F1)-mediated knockdown efficiency.
- (F) Western blot and analysis of protein levels following siE2F1 treatment.
- (G and H) Western blot of EZH2-E2F1-p-Rb pathway in SU.86.86 and Capan-1 cells treated with L-Glu and DRG CM treatment (G) and upstream regulators of EZH2 in SU.86.86 cells treated with L-Glu (10 min) following CaMK IV siRNA pretreatment (H). CREB and p-CREB (Ser133) indicate CREB1 and pCREB1 Ser133, respectively.
- (I) L-Glu dose-response curves of SU.86.86 cells co-cultured with hSPCs-01, showing normalized area under the curve (Norm. AUC) and peak amplitude; n = 6 for each dose (0.1 mM, 0.3 mM, 1.0 mM, and 3.0 mM).
- (J) Brightfield image (63x) of two SU.86.86 cells in hSPCs-01 co-culture (red box), with corresponding Fura2 signals, adjacent to the L-Glu puffing electrode (blue arrow). Scale bars, 50 µm.

(K and L) Calcium responses of SU.86.86 cells in hSPCs-SU.86.86 co-culture to varying durations of 1 mM L-Glu puffing (K, n = 3 per duration) and to 1 mM L-Glu with/without different blockers: 10 μ M UBP141 (GRIN2C/2D antagonist), 3 μ M Ro25-6981 (GRIN2B antagonist), 50 μ M AP5 (selective and competitive NMDA receptor antagonist) (L, n = 6/group). x axis, time (s); y axis, Fura-2 ratio (340/380).

(M) Calcium signaling in SU.86.86 mono-cultures under L-Glu and NMDA ligands. x axis and y axis as in (K-L).

All data are mean \pm SEM. Unpaired t test; *p < 0.05, **p < 0.01, ****p < 0.001, ****p < 0.0001. Also see Figure S4.





(A) *Grin2d* mRNA and GRIN2D protein in non-targeting shRNA (shNT)-treated and *Grin2d*-targeting shRNA (sh*Grin2d*; #210 and #213)-treated KPC-Pdx1CRE cells; sh*Grin2d* (#210) for follow-up.



intraperitoneally on postnatal day 2 (P2) for sensory nerve depletion (Figure 6A). Notably, a significant reduction in tumor volume was observed at the experimental endpoint in the *Grin2d*^{-/-} group, resulting in decreased pancreas weight. Importantly, exogenous (i.p.) glutamate supply reversed the tumor reduction in capsaicin-treated mice only when *Grin2d* was intact (*Grin2d*^{+/+}), with no increase in tumor size observed in solvent-treated controls (Figures 6B, 6C, S8A, and S8B). Moreover, P2 mice treated with capsaicin had a reduction in the neuron density in their T8-T12 DRG during adulthood (Figure 6D). Ablation of sensory fibers was further demonstrated by reduced TRPV1 and NF200 density in T8-T12 DRGs (Figure 6E) and a corresponding decrease of TRPV1⁺ or NF200⁺ nerve fibers in tumor tissues following capsaicin treatment (Figure 6F).

Moreover, we investigated the effect of sensory neuron ablation on PDAC progression using Trpv1 KO mice. In line with the observed pro-neurogenic effects of TGFA in our Grin2d^{-/-} KPC-Pdx1CRE implantation model, a decrease in TGFA secretion in the supernatant and cell lysates from Trpv1 KO DRG neurons was observed compared to Trpv1 WT neurons, accompanied by reduced L-Glu levels (Figures S9A and S9B). Although co-culturing with KPC-Pdx1CRE and TPAC cells enhanced TGFA release from Trpv1 KO DRGs, secretion levels remained lower than those in co-cultures with Trpv1 WT DRGs. Notably, KPC-Pdx1CRE cells exhibited increased extracellular TGFA secretion when co-cultured with Trpv1 WT DRGs, compared to TPAC cells, despite the latter showing a higher baseline TGFA secretion. This was accompanied by a more pronounced increase in intracellular TGFA levels within the KPC-Pdx1CRE cells (Figure S9B). To enhance the neuro-affinity of cancer cells, we stably overexpressed murine Tafa gene under the EF1a promoter in Grin2d+/+ and Grin2d-/- KPC-Pdx1CRE cells. The overexpression of Tgfa in the generated Grin2d+/+;Tgfa-Tg and Grin2d-/-;Tgfa-Tg KPC-Pdx1CRE cell lines was confirmed by western blot, showing a significant increase in TGFA protein levels (Figure 6G), KPC-Pdx1CRE cells exhibited neuro-affine growth capabilities similar to TPAC cells and demonstrated greater invasiveness toward WT DRGs compared to KPC cell lines in 3D migration assay, a feature further enhanced by upregulated Tgfa expression. However, this capability was significantly reduced toward Trpv1 KO DRGs (Figure S9C).

Next, we orthotopically implanted cancer cells with or without Tgfa overexpression into the pancreas of Trpv1 KO and C57BL/6N wild-type mice (6–8 weeks old, both sexes), generating four experimental groups: $Grin2d^{+/+}$, $Grin2d^{-/-}$, $Grin2d^{+/+}$;Tgfa-Tg, and $Grin2d^{-/-}$;Tgfa-Tg (Figure 6H). At the study endpoint, although the $Grin2d^{+/+}$;Tgfa-Tg group in Trpv1 KO mice exhibited significantly larger tumors compared to the $Grin2d^{+/+}$ group, their tumor volumes remained markedly lower than those in the Trpv1 WT $Grin2d^{+/+}$;Tgfa-Tg group, which showed the

most pronounced tumor growth (Figure 6I). Furthermore, we quantified pain sensation in our experimental mice following sensory neuron ablation via von Frey filament testing. Trpv1 WT mice exhibited significantly higher baseline sensitivity to mechanical stimulation with Von Frey filaments compared to Trpv1 KO mice. Following orthotopic implantation in Trpv1 WT mice, compared to Grin2d^{-/-};Tgfa-Tg group, those transplanted with Grin2d+/+;Tgfa-Tg cells developed larger tumors and demonstrated elevated mechanical pain sensitivity. The increase in pain sensation was more pronounced than that observed in Trpv1 KO mice implanted with the same gene-edited cells and also exceeded the baseline sensitivity in Trpv1 WT mice prior to implantation. Notably, Trpv1 KO mice did not exhibit a comparable increase in pain sensitivity following tumor implantation, suggesting a Trpv1-dependent mechanism underlying tumorassociated mechanical pain (Figure 6J).

To further elucidate the feedforward loop via TGFA-EGFR signaling, two predicted binding sites of EZH2 within the Tgfa promoter were identified (Figures S9D and S9E). Silencing Ezh2 significantly reduced its enrichment at the Tafa promoter in KPC-Pdx1CRE cells, as demonstrated by ChIP-PCR analysis. The reduction in EZH2 enrichment at the same sites was further corroborated in Grin2d^{-/-} KPC-Pdx1CRE cells (Figures S9F and S9G). Depletion of Grin2d and its upstream regulator Ezh2 suppressed the expression levels of signal transduction molecules of EZH2-GRIN2D-TGFA signaling pathway, including EGFR. E2F1, pCREB1^{Ser133}, and TGFA in KPC-Pdx1CRE cells (Figure S9H). Notably, exogenous L-Glu application failed to fully restore the reductions in E2F1 and pCREB1 Ser133 caused by Grin2d or Ezh2 depletion, while TGFA levels showed partial recovery. In contrast, in siNT or Grin2d+/+ KPC-Pdx1CRE cells, these signaling proteins were robustly upregulated in response to glutamate stimulation (Figures S9I and S9J).

To better explore the involvement of calcium channels in the functional activity of GRIN2D-containing NMDA receptors, our RNA-seg analysis revealed that Grin2d KO in the murine pancreatic cancer cells led to downregulation of Cacna1h (Cav3.2, T-type calcium channel) and upregulation of Cacna1c (Cav1.2, L-type calcium channel) genes (Figure S9K). Correspondingly, calcium imaging revealed a complete loss of calcium influx in Grin2d-/- cells, in contrast to robust influx in Grin2d+/+ cells (Figure S9L). This suggests that reduced Cacna1h expression functionally impairs calcium entry. Given Cacna1h's role in lowthreshold, transient calcium influx, 52,53 its loss likely accounts for the observed signaling defect in spite of Cacna1c upregulation. Cancer cells frequently exhibit spontaneous calcium influx and membrane depolarization mediated by L-type and T-type voltage-dependent calcium channels (VdCCs), which have been observed in postsynaptic PDAC cells co-cultured with neurons. NMDA receptor activation depends on glutamate binding,

⁽B) Schematic and gel verification of Grin2d gene editing in KPC-Pdx1CRE cells with corresponding GRIN2D protein levels.

⁽C) Schematic of orthotopic implantation model.

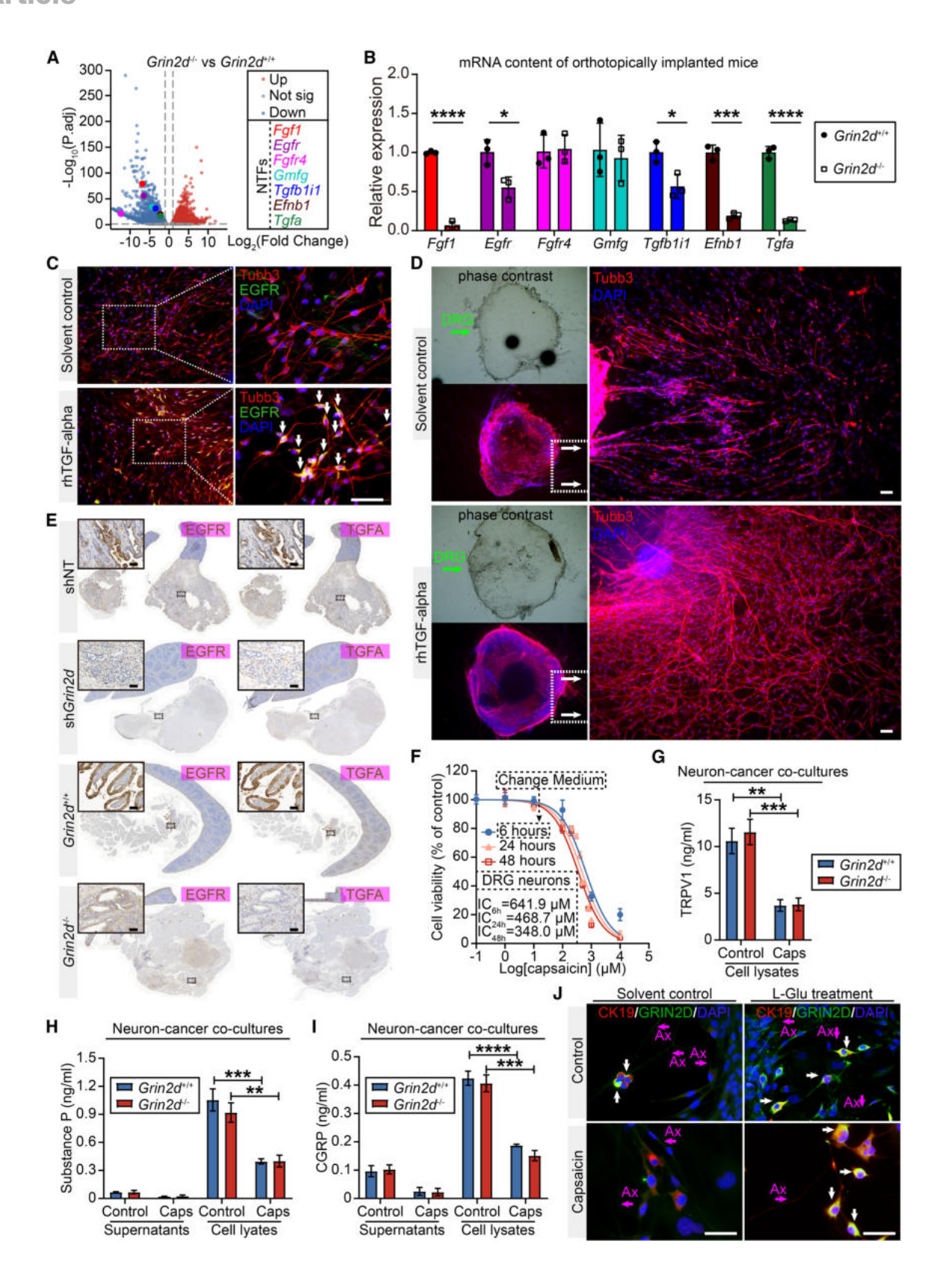
⁽D) Survival of orthotopically implanted sh*Grin2d* and *Grin2d*^{-/-} cohorts and their controls. Statistical analysis was performed using log rank (Mantel-Cox) test. (E) Ultrasonography-based volumes of orthotopic tumors.

⁽F and G) Glutamate levels in tumors (F) and T8-T12 DRGs (G) of implanted Grin2d-modified mice.

⁽H and I) Immunofluorescence of cleaved caspase 9 (Cas9-cleaved) (H) and PGP9.5 (innervation), GRIN2D, EZH2, and CaMK4 (I) in tumors of implanted mice. Scale bars, 20 µm.

⁽A and E-G): data shown as mean ± SEM. Unpaired t test, *p < 0.05, **p < 0.01, ***p < 0.001, ****p < 0.0001. Also see Figures S5 and S6.





(legend on next page)



which may originate from localized release at specialized microdomains, i.e., "pseudo-synapses" (reminiscent of tripartite synapses²⁸). NMDA receptors activation enables additional independent calcium currents.54 The spontaneous calcium influx activity by VdCCs leads to depolarization and enables the easier release of the Mg²⁺ block within NMDA receptors. Such spatially restricted glutamatergic signaling in tumor contexts enables localized NMDA receptor activation and downstream calcium signaling. These findings support a model in which spontaneous depolarization through VdCCs lowers the activation threshold for NMDA receptors by relieving Mg²⁺ block, in which GRIN2D-containing NMDA receptors mediate a glutamate-dependent calcium influx that complements baseline-voltage-dependent calcium signaling in pancreatic cancer cells. These findings indicate that Grin2d regulates calcium homeostasis through Cacna1h, with potential consequences for KPC-Pdx1CRE cell behavior. Further analysis of the TCGA dataset revealed that high CACNA1H expression was significantly associated with improved overall survival in PDAC patients (Figure S9M).

Sensory neurons supply glutamate to pancreatic cancer cells in human PDAC via neuron-cancer pseudo-synapses

Finally, we began to investigate whether glutamate released by neurons can activate NMDARs in pancreatic cancer cells through a pseudo-synaptic signaling. To analyze this hypothesis, we examined patient-derived PDAC specimens for the presence of synaptic structures using transmission electron microscopy (TEM). TEM scans revealed both types of neural invasion, i.e., endoneural and perineural invasion (Figures 7A and S10A). Notably, scattered and distinctly distributed nerve axons (Ax) were observed around the cancer cells (Figures 7Aa1 and 7Aa2), forming the foundational prerequisite for neuron-cancer pseudo-synaptic structures. Furthermore, we found a high density of presynaptic boutons contacting the invading cancer cells with both large dense core vesicles (arguably containing neuropeptides) and small synaptic vesicles (indicative of molecular neurotransmitters, such as glutamate) (Figure 7Ab).

As a key finding, in our human PDAC samples, a highly organized, dark, electron-dense area on the postsynaptic membrane, identified as the postsynaptic density (PSD), was clearly visible (Figures 7B1–7B3). This is in line with the ultrastructure of excitatory synapses known from the CNS, suggesting the concentration of postsynaptic receptors on the cancer cell membrane, and that the neuronal presynapse connecting to the postsynaptic GRIN2D is equipped with components of the release & receive machinery.

Axo-axonic synapses in a healthy nerve are rare and can be only occasionally observed in transversal sections of a nerve⁵⁵; however, we identified numerous neuron-cancer pseudo-synapses at the site of neural invasion, even within smaller nerves on a single cross-section (Figure 7B). TEM images further demonstrated the immunogold staining of GRIN1 and SLC17A6 in these neuron-cancer pseudo-synapses (Figure 7C).

To quantify the potential pseudo-synaptic sites, we measured the co-localization sites of GRIN2D, PANCK, and SLC17A6 in 19 patient-derived PDAC specimens, which resulted in an average of 43.02 \pm 6.96 pseudo-synapses/mm² (Figures S10B–S10D). Additionally, we observed an increase in the number of potential tumor pseudo-synaptic sites, quantified by co-localization of DLG4, CK19, and SLC17A6, in mice orthotopically implanted with $Grin2d^{+/+}$ -KPC-Pdx1CRE cells compared to those implanted with $Grin2d^{-/-}$ -KPC-Pdx1CRE cells (19.00 \pm 2.36 vs. 9.71 \pm 1.77, pseudo-synapses/mm²) (Figures S10E and S10F). Moreover, synaptic markers DLG4, VAMP1, and SLC17A6 were significantly less expressed within $Grin2d^{-/-}$ -KPC-Pdx1CRE tumors than in $Grin2d^{+/+}$ -KPC-Pdx1CRE tumors (Figures S10G and S10H).

In line with the TEM analysis on human PDAC specimens, we further observed neuron-cancer pseudo-synapses in vitro between axons extending from neurons, transfected with Slc17a6-RFP, and SU.86.86 cancer cells transfected with GRIN2D-GFP. These pseudo-synapses displayed a scattered distribution of SLC17A6 surrounding neuron-cancer contact sites (Figures S10I1 and S10I2). Further supporting our hypothesis in vitro, scanning electron microscopy (SEM) revealed pseudo-synapses formed by terminal axons and cancer cells (Figure 7Da). Here, neuronal axons enclosed and terminated on cancer cells, while cancer cells were adjacent to the synaptic cleft between pre- and postsynaptic neurons, forming neuroncancer pseudo-synapses (Figure 7Db), which is further depicted in a three-dimensional (3D) reconstruction video (Video S1). Notably, neuronal SLC17A6 red puncta were intimately associated with SU.86.86 GRIN2D-GFP expression, depicting the sites of neuron-cancer pseudo-synapses (Figure 7E). Overall, our findings offer compelling evidence that neurons and pancreatic cancer cells establish pseudo-synapses to facilitate the delivery of neuronal glutamate to cancer cells (Figure 7F).

DISCUSSION

Inspired by the pivotal role of synaptic glutamate signaling in primary and metastatic cancers of the central nervous system, ^{27–29} as well as the prognostic significance of NI in peripheral cancers, ^{11,16–18} our study aimed to explore whether a similar

Figure 5. Impact of GRIN2D knockout in cancer cells on peritumoral neuritogenesis

(A and B) Volcano plot of differential gene expression (A) and RT-qPCR of top seven neurotrophic factors (NTFs) (B) in Grin2d^{-/-} tumors and controls.

(C and D) Immunostaining of EGFR (C) and Tubb3 (β-III-tubulin) (D) in murine DRG cultures with/without recombinant human TGF-alpha (rhTGF-alpha) treatment, depicting differential axon-/neuritogenesis. Scale bars, 50 μm.

(E) Immunostaining of EGFR and TGFA in $\textit{Grin2d}^{-/-}$ tumors and controls. Scale bars, 20 μm .

(F) Viability of DRG neurons under capsaicin treatment.

(G-I) ELISA of TRPV1 (G), substance P (H), and CGRP (I) in supernatants and lysates of neuron-cancer co-cultures with capsaicin (Caps)-pretreated DRGs and Grin2d-modified KPC-Pdx1CRE cells.

(J) Immunostaining of CK19 and GRIN2D in KPC-Pdx1CRE-DRG co-cultures with L-glutamate (L-Glu) and capsaicin treatments. "Ax" indicates axons. Scale bars, 50 μ m. All data are mean \pm SEM, n = 3. Unpaired t test; *p < 0.05, **p < 0.01, ***p < 0.001, ****p < 0.0001. Also see Figure S7.



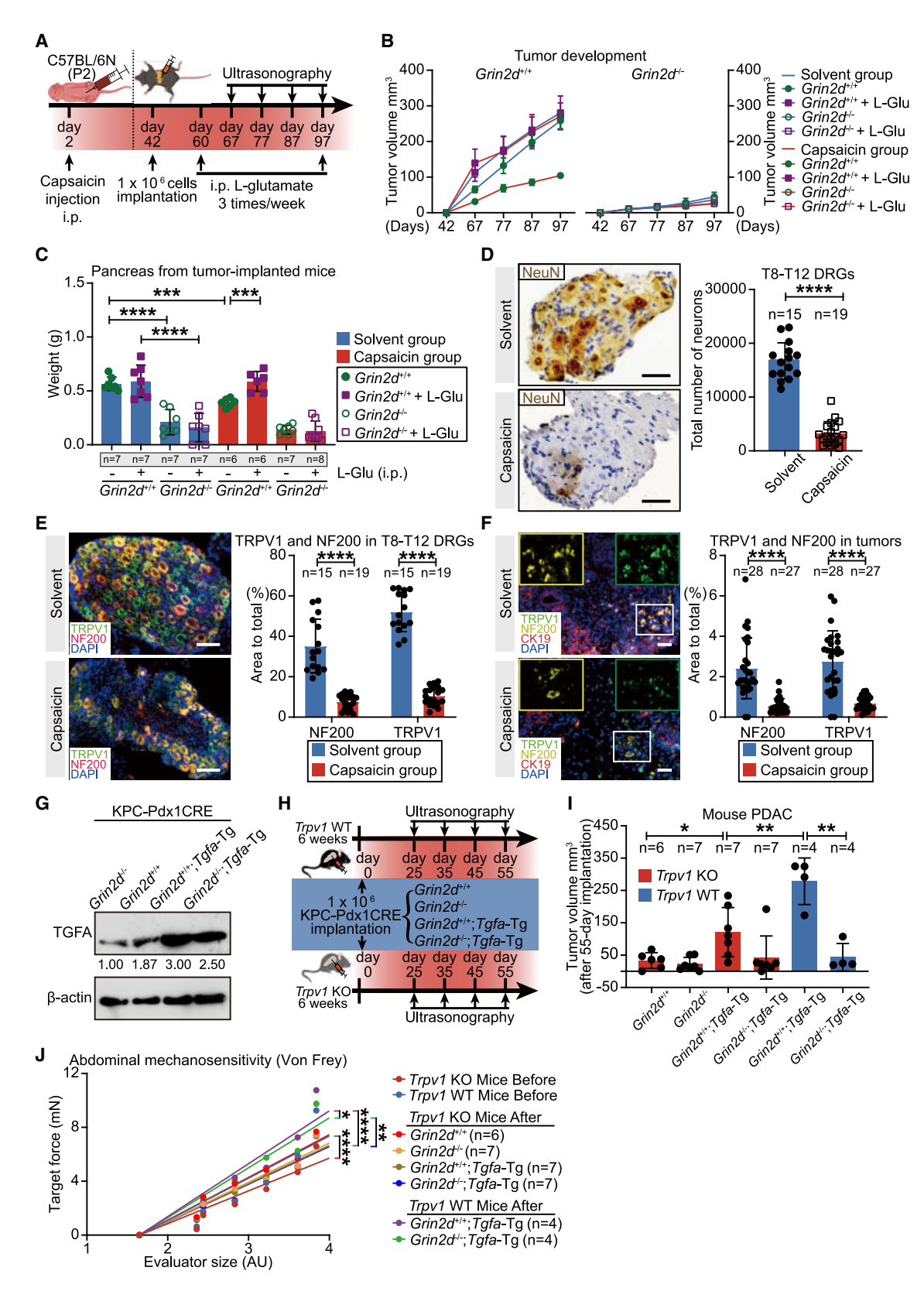


Figure 6. Impact of *GRIN2D* knockout in cancer cells after sensory neuron ablation
(A) Schematic of orthotopic implantation following capsaicin-induced sensory neuron ablation.
(B and C) Tumor volumes measured by ultrasonography (B) and weights (C) of *Grin2d*^{-/-} orthotopic tumors.



mechanism operates between peripheral nerves and cancers outside the brain. Our findings not only demonstrate the existence of synaptic signaling between sensory neurons and pancreatic cancer cells but also highlight the critical role of this axis in tumor growth and spread. Specifically, we identified glutamate-mediated, pseudo-synaptic nerve-cancer interactions as a fundamental driver of pancreatic cancer progression, mediated by the NMDA receptor subunit GRIN2D. Leveraging data from TCGA databases, we corroborated these findings, highlighting the widespread relevance of *GRIN2D* across multiple human cancers.

Glutamate-NMDAR signaling has been previously shown to be involved in cancer growth and to affect prognosis of cancer patients. ^{26,56} Li et al. ⁵⁶ showed that GKAP, a scaffold protein of NMDAR, impacted on the invasiveness of tumor cells derived from pancreatic neuroendocrine tumors and of PDAC, and several cancers with a low expression for NMDAR-GKAP in their transcriptome associated with a favorable prognosis. Here, the autocrine effects of glutamate were mainly mediated by the GRIN2B subunit of the NMDAR. Furthermore, Li et al. also found that increased interstitial fluid pressure induced autologous glutamate secretion, which subsequently activated NMDAR and its downstream MEK-MAPK and CaMK effectors, thereby promoting invasiveness in several cancers. ²⁶

In the light of these previous findings by Li et al. ²⁶ on the key role of autocrine glutamate signaling over GRIN2B, and of our findings on the synaptic and paracrine effects of glutamate over GRIN2D on PDAC cells, there seem to exist two potential mechanisms over which glutamate-NMDAR can promote cancer cell invasiveness. The co-existence of such an autocrine and a synaptic/paracrine mechanism in the same tumor can be attributable to the well-known molecular and cellular heterogeneity of PDAC but also underscores the translational, therapeutic potential in targeting NMDAR signaling in PDAC.

Although the idea of pancreatic cancer cells becoming "electrically active" when connected to neuronal networks is intriguing, we emphasize that pancreatic cancer cells express GRIN2D-containing NMDA receptors not for canonical synaptic transmission. Rather, they exploit glutamate from neurons as a growth- or survival-promoting signal within glutamate-rich neural niches, enabling context-dependent calcium influx and downstream signaling only when glutamate is locally available at a spatial microdomain, i.e., the pseudo-synapse-thus providing a conditional, energetically efficient advantage. In line with the nature of the GRIN2D subunit, low Mg2+ block and slow deactivation kinetics of this subunit allows response to ambient or low-level glutamate, and high glutamate sensitivity enables detection of even diffuse glutamate release. Although NMDA receptors are energy-demanding, their activation is conditional, only occurring in the presence of extracellular glutamate—not a default open channel. In return, they provide survival or pro-invasive signals, possibly through Ca²⁺-dependent gene expression. This is also in analogy with breast cancer metastasis in the brain, ²⁸ where the cancer cells expressing glutamate receptors (including NMDA) exhibit enhanced proliferation, migration, and stemness, but no real action potentials or electrical activity. One can regard the function of the herein described "pseudo-synapses" from a strategic point of view for the cancer cells, where NMDA receptors may act as "conditional biosensors" rather than constant signal conduits, which minimizes energetic burden, while enabling contextual advantages like neuroinvasion or tumor progression.

Although our functional data focused mainly on PDAC, we have shown that GRIN2D expression increases in numerous other peripheral cancers. Considering the known tumor-supporting role NI plays in some of these cancers, ^{57–59} it remains for further investigation to study whether the herein-described pseudo-synaptic sensory neuron-cancer axis is a driving factor in other peripheral cancers as well. Taken together with the findings of Li et al., ⁵⁶ our study refines the model of NMDAR signaling in PDAC: GRIN2B-GKAP mediates glutamate-driven autocrine signaling, while GRIN2D mediates neuron-derived, paracrine signaling. Both contribute to cancer aggressiveness through complementary yet spatially distinct mechanisms, together offering a broader and more nuanced framework for understanding NMDAR-dependent tumor biology in pancreatic cancer.

We envision that our findings could lead to the development of oncological therapies instructed by cancer neuroscience, leveraging non-blood-brain-barrier-penetrating pharmacological GRIN2D-NMDAR inhibitors to target this pathway with potentially wide therapeutic windows and minimal adverse effects on the central nervous system.

RESOURCE AVAILABILITY

Lead contact

Further information and requests for resources should be directed to the lead contact, Ihsan Ekin Demir (ekin.demir@tum.de).

Materials availability

This study did not generate new unique reagents.

Data and code availability

Public datasets used in this study include pan-cancer and pancreatic adeno-carcinoma (PAAD) datasets from TCGA, available through the Genomic Data Commons (https://portal.gdc.cancer.gov/); the scRNA-seq dataset GSE202051, available from the Gene Expression Omnibus (GEO); and scRNA-seq dataset from the Human Tumor Atlas Network (HTAN) dbGaP Study phs002371.v1.p1 (https://www.ncbi.nlm.nih.gov/projects/gap/cgi-bin/study.cgi?study_id=phs002371.v1.p1). The RNA-seq data generated from this study have been deposited with GEO under accession code GSE291933. The raw data will be made available upon request.

⁽D) Immunostaining for NeuN showing significant loss of T8-T12 DRG neurons post-capsaicin, quantified by total number of neurons. Scale bars, 20 μ m. (E and F) Immunostaining and analysis of TRPV1 and NF200 in T8-T12 DRGs (E) and tumors (F) of implanted mice following sensory neuron ablation via capsaicin treatment. Scale bars, 20 μ m.

⁽G) TGFA transfection efficiency in *Grin2d*^{+/+} and *Grin2d*^{-/-} KPC-Pdx1CRE cell lines.

⁽H) Schematic of orthotopic implantation in Trpv1 knockout (KO) and wild-type (WT) mice.

⁽l) Ultrasonography-based volumes of gene-edited KPC-Pdx1CRE orthotopic tumors: $Grin2d^{+/+}$, $Grin2d^{-/-}$

⁽J) Von Frey test of mechanical sensitivity in Trpv1 WT/KO mice pre-implantation and day 55 post-implantation.

⁽B–F and I–J) Data shown as mean \pm SEM. Unpaired t test; *p < 0.05, **p < 0.01, ***p < 0.001, ****p < 0.0001. Also see Figures S8 and S9.



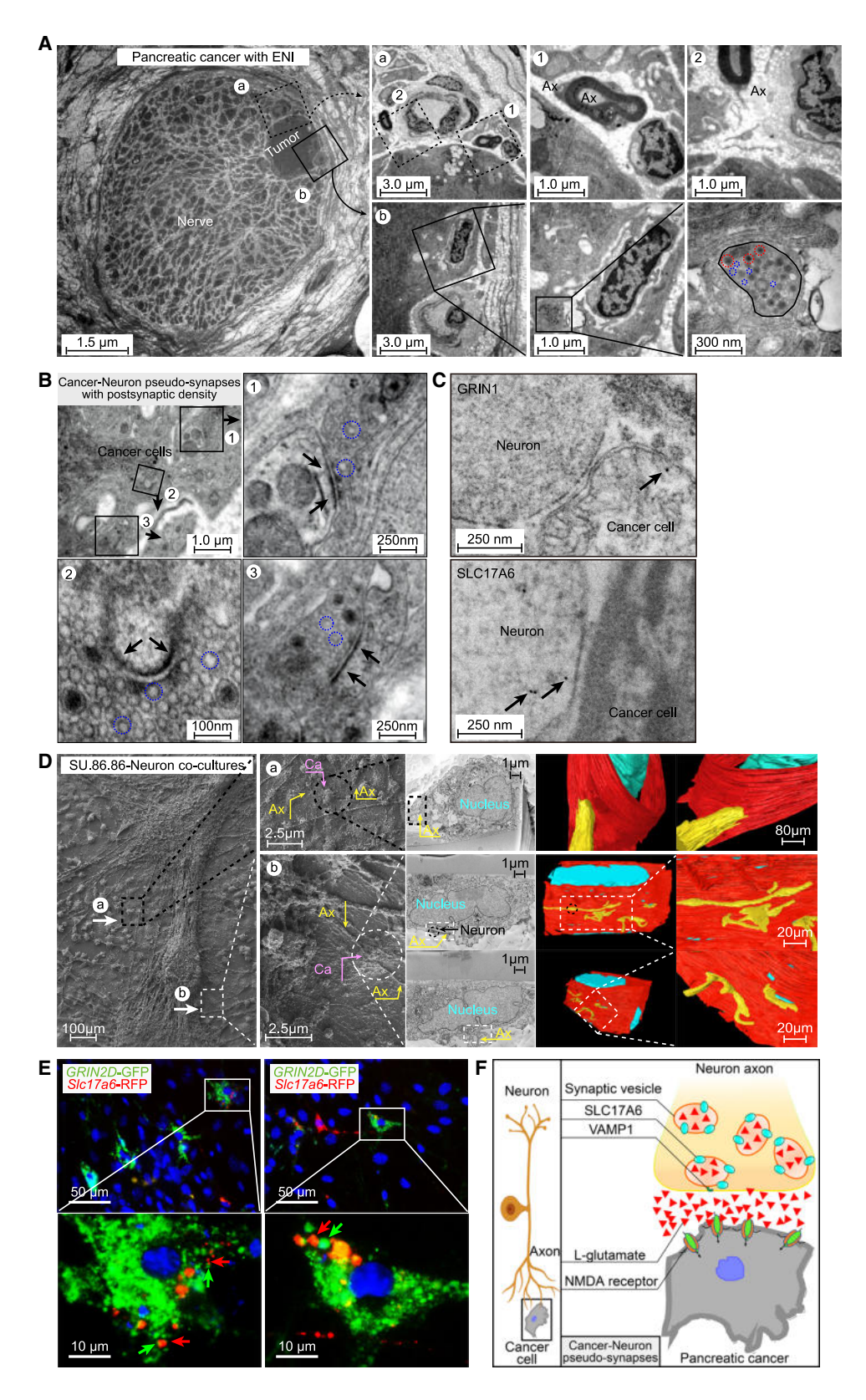


Figure 7. Pseudo-synaptic interaction between PDAC cells and neurons

(A) Transmission electron microscopy (TEM) of human PDAC endoneural invasion (ENI) showing axons (Ax) around cancer cells (a), presynaptic bouton (black solid outline), dense core vesicles (red dotted circle), and synaptic vesicles (blue dotted circle) with neurotransmitters-L-glutamate (b).



Cancer Cell **Article**

ACKNOWLEDGMENTS

Grant support: I.E.D. and L.R. were supported by a grant of the Deutsche Forschungsgemeinschaft (DFG, German Research Foundation)-Project-ID DE 2428/11-1. I.E.D. was supported by the Else Kröner Clinician Scientist Professorship Program of the Else Kroner-Fresenius Foundation. The sensory neuron and pup illustrations were created with BioRender.com.

AUTHOR CONTRIBUTIONS

I.E.D. and L.R. designed the study. L.R., C.L., and S.T. performed the experiments and/or analyzed the data. L.R., C.M.R., and S.T. supported the implantation experiments. L.R., A.K., K.G., P.H.N., and U.M. performed the electron microscopy studies. S.E.Y., U.S., M.I.M.A., and V.T. performed bioinformatical analysis of RNA-seq data; L.R., K.C., R.I., and I.E.D. wrote the manuscript. L.R., M.B., and G.R. performed calcium measurements and patch-clamp experiments. I.E.D. supervised the study. All authors have approved the final version of the manuscript.

DECLARATION OF INTERESTS

The authors declare no conflict of interest.

STAR*METHODS

Detailed methods are provided in the online version of this paper and include the following:

- KEY RESOURCES TABLE
- EXPERIMENTAL MODEL AND STUDY PARTICIPANT DETAILS
 - o Patient samples
 - o Cell lines and cell culture
 - Mouse experiments
- METHOD DETAILS
 - Migration assay with time-lapse microscopy
 - o Ablation of sensory fibers for the tumor growth following KPC-Pdx1CRE cell implantation
 - o Cell treatments, wound healing assay, colony formation assay, MTT assav, and cell invasion assav
 - o Immunocytochemical (ICC), immunohistochemical (IHC), and immunofluorescent (IF) staining
 - o Gene editing
 - o Real-time quantitative PCR (RT-qPCR) and chromatin immunoprecipitation (ChIP)-PCR assay
 - o Western blot and ELISA
 - o Inhibitors and recombinant proteins
 - o Bioinformatic analysis
 - o Scanning & transmission electron microscopy
 - o Calcium signal (Ca-signal) imaging
 - Von Frey test
- QUANTIFICATION AND STATISTICAL ANALYSIS

SUPPLEMENTAL INFORMATION

Supplemental information can be found online at https://doi.org/10.1016/j. ccell.2025.09.003.

Received: August 24, 2024 Revised: March 19, 2025 Accepted: September 8, 2025

REFERENCES

- 1. Storz, P., and Crawford, H.C. (2020). Carcinogenesis of Pancreatic Ductal Adenocarcinoma. Gastroenterology 158, 2072-2081. https://doi.org/10. 1053/j.gastro.2020.02.059.
- 2. Christenson, E.S., Jaffee, E., and Azad, N.S. (2020). Current and emerging therapies for patients with advanced pancreatic ductal adenocarcinoma: a bright future. Lancet Oncol. 21, e135-e145. https://doi.org/10.1016/ s1470-2045(19)30795-8.
- 3. Rahib, L., Smith, B.D., Aizenberg, R., Rosenzweig, A.B., Fleshman, J.M., and Matrisian, L.M. (2014). Projecting cancer incidence and deaths to 2030: the unexpected burden of thyroid, liver, and pancreas cancers in the United States. Cancer Res. 74, 2913-2921. https://doi.org/10.1158/ 0008-5472.Can-14-0155.
- 4. Siegel, R.L., Miller, K.D., Fuchs, H.E., and Jemal, A. (2021). Cancer Statistics, 2021. CA Cancer J. Clin. 71, 7-33. https://doi.org/10.3322/
- 5. Siegel, R.L., Miller, K.D., and Jemal, A. (2019). Cancer statistics, 2019. CA Cancer J. Clin. 69, 7-34. https://doi.org/10.3322/caac.21551.
- 6. Siegel, R.L., Miller, K.D., and Jemal, A. (2017). Cancer Statistics, 2017. CA Cancer J. Clin. 67, 7-30. https://doi.org/10.3322/caac.21387.
- 7. Scheufele, F., Hartmann, D., and Friess, H. (2019). Treatment of pancreatic cancer-neoadjuvant treatment in borderline resectable/locally advanced pancreatic cancer. Transl. Gastroenterol. Hepatol. 4, 32. https://doi.org/ 10.21037/tgh.2019.04.09.
- 8. Demir, I.E., Friess, H., and Ceyhan, G.O. (2015). Neural plasticity in pancreatitis and pancreatic cancer. Nat. Rev. Gastroenterol. Hepatol. 12, 649-659. https://doi.org/10.1038/nrgastro.2015.166.
- 9. Demir, I.E., Mota Reyes, C., Alrawashdeh, W., Ceyhan, G.O., Deborde, S., Friess, H., Görgülü, K., Istvanffy, R., Jungwirth, D., Kuner, R., et al. (2021). Future directions in preclinical and translational cancer neuroscience research. Nat. Cancer 1, 1027-1031. https://doi.org/10.1038/s43018-
- 10. Demir, I.E., Reyes, C.M., Alrawashdeh, W., Ceyhan, G.O., Deborde, S., Friess, H., Görgülü, K., Istvanffy, R., Jungwirth, D., Kuner, R., et al. (2020). Clinically Actionable Strategies for Studying Neural Influences in Cancer Cell 38, 11-14. https://doi.org/10.1016/j.ccell.2020.
- 11. Ren, L., Jäger, C., Schorn, S., Pergolini, I., Göß, R., Safak, O., Kießler, M., Martignoni, M.E., Novotny, A.R., Friess, H., et al. (2023). Arterial Resection for Pancreatic Cancer: Feasibility and Current Standing in a High-Volume Center. Ann. Surg. Open. 4, e302. https://doi.org/10.1097/as9. 0000000000000302.
- 12. Deborde, S., Omelchenko, T., Lyubchik, A., Zhou, Y., He, S., McNamara, W.F., Chernichenko, N., Lee, S.Y., Barajas, F., Chen, C.H., et al. (2016). Schwann cells induce cancer cell dispersion and invasion. J. Clin. Investig. 126, 1538-1554. https://doi.org/10.1172/jci82658.
- 13. Deborde, S., and Wong, R.J. (2017). How Schwann cells facilitate cancer progression in nerves. Cell. Mol. Life Sci. 74, 4405-4420. https://doi.org/ 10.1007/s00018-017-2578-x.

⁽B) Cancer-neuron pseudo-synapses at the human PDAC invasion site; visible postsynaptic density (PSD, black arrows) and synaptic vesicles (blue dotted circle) containing neurotransmitters like L-glutamate.

⁽C) TEM immunogold labeling of GRIN1 and SLC17A6 at cancer-neuron pseudo-synapses.

⁽D) Scanning electron microscopy (SEM) of SU.86.86-DRG co-cultures, capturing pseudo-synapses (a) and axons enclosing and ending on cancer cells (Ca) (b). Red: cell membrane; yellow: axon (Ax); bright light blue: nucleus. See Video S1.

⁽E) Confocal images of cancer-neuron pseudo-synapses at cancer GRIN2D-GFP (green arrowheads) and neuronal SIc17a6-RFP (red arrowheads) sites in co-cultures.

⁽F) Schematic of sensory neuron-PDAC pseudo-synapses. Also see Figure S10 and Video S1.



- Yurteri, Ü., Çifcibaşı, K., Friess, H., Ceyhan, G.O., Istvanffy, R., and Demir, I.E. (2022). Schwann Cells in Peripheral Cancers: Bystanders or Promoters? Adv. Biol. 6, e2200033. https://doi.org/10.1002/adbi. 202200033.
- Demir, I.E., Friess, H., and Ceyhan, G.O. (2012). Nerve-cancer interactions in the stromal biology of pancreatic cancer. Front. Physiol. 3, 97. https://doi.org/10.3389/fphys.2012.00097.
- Schorn, S., Demir, I.E., Haller, B., Scheufele, F., Reyes, C.M., Tieftrunk, E., Sargut, M., Goess, R., Friess, H., and Ceyhan, G.O. (2017). The influence of neural invasion on survival and tumor recurrence in pancreatic ductal adenocarcinoma - A systematic review and meta-analysis. Surg. Oncol. 26, 105–115. https://doi.org/10.1016/j.suronc.2017.01.007.
- Badger, S.A., Brant, J.L., Jones, C., McClements, J., Loughrey, M.B., Taylor, M.A., Diamond, T., and McKie, L.D. (2010). The role of surgery for pancreatic cancer: a 12-year review of patient outcome. Ulst. Med. J. 79, 70-75.
- Chen, J.W.C., Bhandari, M., Astill, D.S., Wilson, T.G., Kow, L., Brooke-Smith, M., Toouli, J., and Padbury, R.T.A. (2010). Predicting patient survival after pancreaticoduodenectomy for malignancy: histopathological criteria based on perineural infiltration and lymphovascular invasion. HPB (Oxford) 12, 101–108. https://doi.org/10.1111/j.1477-2574.2009.00140.x.
- Amit, M., Na'ara, S., and Gil, Z. (2016). Mechanisms of cancer dissemination along nerves. Nat. Rev. Cancer 16, 399–408. https://doi.org/10.1038/nrc.2016.38
- Jobling, P., Pundavela, J., Oliveira, S.M.R., Roselli, S., Walker, M.M., and Hondermarck, H. (2015). Nerve-Cancer Cell Cross-talk: A Novel Promoter of Tumor Progression. Cancer Res. 75, 1777–1781. https://doi.org/10. 1158/0008-5472.Can-14-3180.
- Çifcibaşı, K., Mota Reyes, C., Istvanffy, R., and Demir, I.E. (2023). In Cancer Neuroscience, M. Amit and N.N. Scheff, eds. (Springer International Publishing), pp. 117–129.
- Stopczynski, R.E., Normolle, D.P., Hartman, D.J., Ying, H., DeBerry, J.J., Bielefeldt, K., Rhim, A.D., DePinho, R.A., Albers, K.M., and Davis, B.M. (2014). Neuroplastic changes occur early in the development of pancreatic ductal adenocarcinoma. Cancer Res. 74, 1718–1727. https://doi.org/10. 1158/0008-5472.Can-13-2050.
- Saloman, J.L., Albers, K.M., Li, D., Hartman, D.J., Crawford, H.C., Muha, E.A., Rhim, A.D., and Davis, B.M. (2016). Ablation of sensory neurons in a genetic model of pancreatic ductal adenocarcinoma slows initiation and progression of cancer. Proc. Natl. Acad. Sci. USA *113*, 3078–3083. https://doi.org/10.1073/pnas.1512603113.
- Hirth, M., Gandla, J., Höper, C., Gaida, M.M., Agarwal, N., Simonetti, M., Demir, A., Xie, Y., Weiss, C., Michalski, C.W., et al. (2020). CXCL10 and CCL21 Promote Migration of Pancreatic Cancer Cells Toward Sensory Neurons and Neural Remodeling in Tumors in Mice, Associated With Pain in Patients. Gastroenterology 159, 665–681.e13. https://doi.org/10. 1053/j.gastro.2020.04.037.
- Wang, X., Istvanffy, R., Ye, L., Teller, S., Laschinger, M., Diakopoulos, K. N., Görgülü, K., Li, Q., Ren, L., Jäger, C., et al. (2023). Phenotype screens of murine pancreatic cancer identify a Tgf-α-Ccl2-paxillin axis driving human-like neural invasion. J. Clin. Investig. 133, e166333. https://doi.org/10.1172/jci166333.
- Li, L., and Hanahan, D. (2013). Hijacking the neuronal NMDAR signaling circuit to promote tumor growth and invasion. Cell 153, 86–100. https:// doi.org/10.1016/j.cell.2013.02.051.
- Venkataramani, V., Tanev, D.I., Strahle, C., Studier-Fischer, A., Fankhauser, L., Kessler, T., Körber, C., Kardorff, M., Ratliff, M., Xie, R., et al. (2019). Glutamatergic synaptic input to glioma cells drives brain tumour progression. Nature 573, 532–538. https://doi.org/10.1038/ s41586-019-1564-x.
- Zeng, Q., Michael, I.P., Zhang, P., Saghafinia, S., Knott, G., Jiao, W., McCabe, B.D., Galván, J.A., Robinson, H.P.C., Zlobec, I., et al. (2019). Synaptic proximity enables NMDAR signalling to promote brain metastasis. Nature 573, 526–531. https://doi.org/10.1038/s41586-019-1576-6.

- Venkataramani, V., Yang, Y., Schubert, M.C., Reyhan, E., Tetzlaff, S.K., Wißmann, N., Botz, M., Soyka, S.J., Beretta, C.A., Pramatarov, R.L., et al. (2022). Glioblastoma hijacks neuronal mechanisms for brain invasion. Cell 185, 2899–2917.e31. https://doi.org/10.1016/j.cell.2022.06.054.
- Malet, M., and Brumovsky, P.R. (2015). VGLUTs and Glutamate Synthesis-Focus on DRG Neurons and Pain. Biomolecules 5, 3416– 3437. https://doi.org/10.3390/biom5043416.
- Demir, I.E., Boldis, A., Pfitzinger, P.L., Teller, S., Brunner, E., Klose, N., Kehl, T., Maak, M., Lesina, M., Laschinger, M., et al. (2014). Investigation of Schwann cells at neoplastic cell sites before the onset of cancer invasion. J. Natl. Cancer Inst. 106, dju184. https://doi.org/10. 1093/jnci/dju184.
- Hess, S.D., Daggett, L.P., Deal, C., Lu, C.C., Johnson, E.C., and Veliçelebi, G. (1998). Functional characterization of human N-methyl-D-aspartate subtype 1A/2D receptors. J. Neurochem. 70, 1269–1279. https://doi. org/10.1046/j.1471-4159.1998.70031269.x.
- Hwang, W.L., Jagadeesh, K.A., Guo, J.A., Hoffman, H.I., Yadollahpour, P., Reeves, J.W., Mohan, R., Drokhlyansky, E., Van Wittenberghe, N., Ashenberg, O., et al. (2022). Single-nucleus and spatial transcriptome profiling of pancreatic cancer identifies multicellular dynamics associated with neoadjuvant treatment. Nat. Genet. 54, 1178–1191. https://doi.org/ 10.1038/s41588-022-01134-8.
- Cui Zhou, D., Jayasinghe, R.G., Chen, S., Herndon, J.M., Iglesia, M.D., Navale, P., Wendl, M.C., Caravan, W., Sato, K., Storrs, E., et al. (2022). Spatially restricted drivers and transitional cell populations cooperate with the microenvironment in untreated and chemo-resistant pancreatic cancer. Nat. Genet. 54, 1390–1405. https://doi.org/10.1038/s41588-022-01157-1.
- Engel, A.G. (2018). Congenital Myasthenic Syndromes in 2018. Curr. Neurol. Neurosci. Rep. 18, 46. https://doi.org/10.1007/s11910-018-0852-4.
- Duan, B., Cheng, L., Bourane, S., Britz, O., Padilla, C., Garcia-Campmany, L., Krashes, M., Knowlton, W., Velasquez, T., Ren, X., et al. (2014). Identification of spinal circuits transmitting and gating mechanical pain. Cell 159, 1417–1432. https://doi.org/10.1016/j.cell.2014.11.003.
- Kim, E., and Sheng, M. (2004). PDZ domain proteins of synapses. Nat. Rev. Neurosci. 5, 771–781. https://doi.org/10.1038/nrn1517.
- Vieira, M., Yong, X.L.H., Roche, K.W., and Anggono, V. (2020). Regulation of NMDA glutamate receptor functions by the GluN2 subunits. J. Neurochem. 154, 121–143. https://doi.org/10.1111/jnc.14970.
- Du, L., Fakih, M.G., Rosen, S.T., and Chen, Y. (2020). SUMOylation of E2F1 Regulates Expression of EZH2. Cancer Res. 80, 4212–4223. https://doi.org/10.1158/0008-5472.Can-20-1259.
- Yao, J.Y., Zhang, L., Zhang, X., He, Z.Y., Ma, Y., Hui, L.J., Wang, X., and Hu, Y.P. (2010). H3K27 trimethylation is an early epigenetic event of p16lNK4a silencing for regaining tumorigenesis in fusion reprogrammed hepatoma cells. J. Biol. Chem. 285, 18828–18837. https://doi.org/10. 1074/jbc.M109.077974.
- Mohammad, F., Weissmann, S., Leblanc, B., Pandey, D.P., Højfeldt, J.W., Comet, I., Zheng, C., Johansen, J.V., Rapin, N., Porse, B.T., et al. (2017). EZH2 is a potential therapeutic target for H3K27M-mutant pediatric gliomas. Nat. Med. 23, 483–492. https://doi.org/10.1038/nm.4293.
- Cao, R., Wang, L., Wang, H., Xia, L., Erdjument-Bromage, H., Tempst, P., Jones, R.S., and Zhang, Y. (2002). Role of histone H3 lysine 27 methylation in Polycomb-group silencing. Science 298, 1039–1043. https://doi.org/10. 1126/science 1076997
- Malínková, V., Vylíčil, J., and Kryštof, V. (2015). Cyclin-dependent kinase inhibitors for cancer therapy: a patent review (2009 - 2014). Expert Opin. Ther. Pat. 25, 953–970. https://doi.org/10.1517/13543776.2015.1045414.
- Hardingham, G.E., and Bading, H. (2010). Synaptic versus extrasynaptic NMDA receptor signalling: implications for neurodegenerative disorders. Nat. Rev. Neurosci. 11, 682–696. https://doi.org/10.1038/nrn2911.
- 45. Ashok, C., Selvam, M., Ponne, S., Parcha, P.K., Raja, K.M.P., and Baluchamy, S. (2020). CREB acts as a common transcription factor for



- major epigenetic repressors; DNMT3B, EZH2, CUL4B and E2F6. Med. Oncol. 37, 68. https://doi.org/10.1007/s12032-020-01395-5.
- Ghosh, K., Chatterjee, B., Maheswari, U., Athifa, M., and Kanade, S.R. (2019).
 4-Nonylphenol-enhanced EZH2 and RNF2 expression, H3K27me3 and H2AK119ub1 marks resulting in silencing of p21 (CDKN1A) in vitro. Epigenomics 11, 899–916. https://doi.org/10.2217/epi-2018-0175.
- Zhang, Y., Zheng, D., Zhou, T., Song, H., Hulsurkar, M., Su, N., Liu, Y., Wang, Z., Shao, L., Ittmann, M., et al. (2018). Androgen deprivation promotes neuroendocrine differentiation and angiogenesis through CREB-EZH2-TSP1 pathway in prostate cancers. Nat. Commun. 9, 4080. https://doi.org/10.1038/s41467-018-06177-2.
- Hingorani, S.R., Wang, L., Multani, A.S., Combs, C., Deramaudt, T.B., Hruban, R.H., Rustgi, A.K., Chang, S., and Tuveson, D.A. (2005). Trp53R172H and KrasG12D cooperate to promote chromosomal instability and widely metastatic pancreatic ductal adenocarcinoma in mice. Cancer Cell 7, 469–483. https://doi.org/10.1016/j.ccr.2005.04.023.
- Kawaguchi, Y., Cooper, B., Gannon, M., Ray, M., MacDonald, R.J., and Wright, C.V.E. (2002). The role of the transcriptional regulator Ptf1a in converting intestinal to pancreatic progenitors. Nat. Genet. 32, 128–134. https://doi.org/10.1038/ng959.
- Jonkers, J., Meuwissen, R., van der Gulden, H., Peterse, H., van der Valk, M., and Berns, A. (2001). Synergistic tumor suppressor activity of BRCA2 and p53 in a conditional mouse model for breast cancer. Nat. Genet. 29, 418–425. https://doi.org/10.1038/ng747.
- Wang, X., Istvanffy, R., Ye, L., Teller, S., Laschinger, M., Diakopoulos, K. N., Görgülü, K., Li, Q., Ren, L., Jäger, C., et al. (2023). Phenotype screens of murine pancreatic cancer identify a Tgf-alpha-Ccl2-paxillin axis driving human-like neural invasion. J. Clin. Investig. 133, e166333. https://doi.org/ 10.1172/JCl166333.
- Melgari, D., Frosio, A., Calamaio, S., Marzi, G.A., Pappone, C., and Rivolta, I. (2022). T-Type Calcium Channels: A Mixed Blessing. Int. J. Mol. Sci. 23, 9894. https://doi.org/10.3390/ijms23179894.
- Autret, L., Mechaly, I., Scamps, F., Valmier, J., Lory, P., and Desmadryl, G. (2005). The involvement of Cav3.2/alpha1H T-type calcium channels in excitability of mouse embryonic primary vestibular neurones. J. Physiol. 567, 67–78. https://doi.org/10.1113/jphysiol.2005.089342.
- Li, J., Xu, Y., Zhu, H., Wang, Y., Li, P., and Wang, D. (2022). The dark side of synaptic proteins in tumours. Br. J. Cancer 127, 1184–1192. https://doi. org/10.1038/s41416-022-01863-x.
- Raudales, R., Kim, G., Kelly, S.M., Hatfield, J., Guan, W., Zhao, S., Paul, A., Qian, Y., Li, B., and Huang, Z.J. (2024). Specific and comprehensive genetic targeting reveals brain-wide distribution and synaptic input patterns of GABAergic axo-axonic interneurons. eLife 13, e93481. https://doi.org/10.7554/eLife.93481.
- Li, L., Zeng, Q., Bhutkar, A., Galván, J.A., Karamitopoulou, E., Noordermeer, D., Peng, M.W., Piersigilli, A., Perren, A., Zlobec, I., et al. (2018). GKAP Acts as a Genetic Modulator of NMDAR Signaling to Govern Invasive Tumor Growth. Cancer Cell 33, 736–751.e5. https://doi. org/10.1016/j.ccell.2018.02.011.
- Barbetta, A., Schlottmann, F., Nobel, T., Sewell, D.B., Hsu, M., Tan, K.S., Gerdes, H., Shah, P., Bains, M.S., Bott, M., et al. (2018). Predictors of Nodal Metastases for Clinical T2N0 Esophageal Adenocarcinoma. Ann. Thorac. Surg. 106, 172–177. https://doi.org/10.1016/j.athoracsur.2018. 02.087.
- Tanaka, A., Matsumura, E., Yosikawa, H., Uchida, T., Machidera, N., Kubo, R., Okuno, K., Koh, K., Watatani, M., and Yasutomi, M. (1998). An evaluation of neural invasion in esophageal cancer. Surg. Today 28, 873–878. https://doi.org/10.1007/s005950050245.
- Abdollahi, A., Zadeh, H.S., Akbari, M., Tahmasbi, S., Talei, A., and Hassanzadeh, J. (2017). Investigation of Prognostic Factors and Survival

- without Recurrence in Patients with Breast Cancer. Adv. Biomed. Res. 6, 42. https://doi.org/10.4103/2277-9175.204595.
- Ceyhan, G.O., Demir, I.E., Altintas, B., Rauch, U., Thiel, G., Müller, M.W., Giese, N.A., Friess, H., and Schäfer, K.H. (2008). Neural invasion in pancreatic cancer: a mutual tropism between neurons and cancer cells. Biochem. Biophys. Res. Commun. 374, 442–447. https://doi.org/10. 1016/j.bbrc.2008.07.035.
- Liebl, F., Demir, I.E., Rosenberg, R., Boldis, A., Yildiz, E., Kujundzic, K., Kehl, T., Dischl, D., Schuster, T., Maak, M., et al. (2013). The severity of neural invasion is associated with shortened survival in colon cancer. Clin. Cancer Res. 19, 50–61. https://doi.org/10.1158/1078-0432.Ccr-12-2392.
- 62. Wang, K., Demir, I.E., D'Haese, J.G., Tieftrunk, E., Kujundzic, K., Schorn, S., Xing, B., Kehl, T., Friess, H., and Ceyhan, G.O. (2014). The neurotrophic factor neurturin contributes toward an aggressive cancer cell phenotype, neuropathic pain and neuronal plasticity in pancreatic cancer. Carcinogenesis 35, 103–113. https://doi.org/10.1093/carcin/bgt312.
- Fangmann, L., Teller, S., Stupakov, P., Friess, H., Ceyhan, G.O., and Demir, I.E. (2018). 3D Cancer Migration Assay with Schwann Cells. Methods Mol. Biol. 1739, 317–325. https://doi.org/10.1007/978-1-4939-7649-2 20.
- Traynelis, S.F., Wollmuth, L.P., McBain, C.J., Menniti, F.S., Vance, K.M., Ogden, K.K., Hansen, K.B., Yuan, H., Myers, S.J., and Dingledine, R. (2010). Glutamate receptor ion channels: structure, regulation, and function. Pharmacol. Rev. 62, 405–496. https://doi.org/10.1124/pr.109. 002451.
- Vivian, J., Rao, A.A., Nothaft, F.A., Ketchum, C., Armstrong, J., Novak, A., Pfeil, J., Narkizian, J., Deran, A.D., Musselman-Brown, A., et al. (2017). Toil enables reproducible, open source, big biomedical data analyses. Nat. Biotechnol. 35, 314–316. https://doi.org/10.1038/nbt.3772.
- Wickham, H. (2016). ggplot2: Elegant Graphics for Data Analysis (Springer-Verlag).
- Wolf, F.A., Angerer, P., and Theis, F.J. (2018). SCANPY: large-scale singlecell gene expression data analysis. Genome Biol. 19, 15. https://doi.org/ 10.1186/s13059-017-1382-0.
- 68. Luckner, M., and Wanner, G. (2018). From Light Microscopy to Analytical Scanning Electron Microscopy (SEM) and Focused Ion Beam (FIB)/ SEM in Biology: Fixed Coordinates, Flat Embedding, Absolute References. Microsc. Microanal. 24, 526–544. https://doi.org/10.1017/ S1431927618015015.
- Kalvelage, J., Wöhlbrand, L., Schoon, R.A., Zink, F.M., Correll, C., Senkler, J., Eubel, H., Hoppenrath, M., Rhiel, E., Braun, H.P., et al. (2023). The enigmatic nucleus of the marine dinoflagellate Prorocentrum cordatum. mSphere 8, e0003823. https://doi.org/10.1128/msphere.00038-23.
- Grupp, L., Wolburg, H., and Mack, A.F. (2010). Astroglial structures in the zebrafish brain. J. Comp. Neurol. 518, 4277–4287. https://doi.org/10. 1002/cne.22481.
- Neckel, P.H., Mattheus, U., Hirt, B., Just, L., and Mack, A.F. (2016). Large-scale tissue clearing (PACT): Technical evaluation and new perspectives in immunofluorescence, histology, and ultrastructure. Sci. Rep. 6, 34331. https://doi.org/10.1038/srep34331.
- Barreto-Chang, O.L., and Dolmetsch, R.E. (2009). Calcium imaging of cortical neurons using Fura-2 AM. J. Vis. Exp. 1067. https://doi.org/10. 3791/1067.
- Demir, I.E., Tieftrunk, E., Schorn, S., Saricaoglu, Ö.C., Pfitzinger, P.L., Teller, S., Wang, K., Waldbaur, C., Kurkowski, M.U., Wörmann, S.M., et al. (2016). Activated Schwann cells in pancreatic cancer are linked to analgesia via suppression of spinal astroglia and microglia. Gut 65, 1001–1014. https://doi.org/10.1136/gutjnl-2015-309784.

Cancer Cell Article



STAR*METHODS

KEY RESOURCES TABLE

REAGENT or RESOURCE	SOURCE	IDENTIFIER
Antibodies		
NMDAR2D Polyclonal Antibody	Thermo Fisher Scientific	Cat# PA5-101608; RRID: AB_2851042
NMDAR1 Polyclonal Antibody	Thermo Fisher Scientific	Cat# PA3-102; RRID: AB_2112003
Synaptobrevin1 antibody	Synaptic Systems	Cat# 104002, RRID: AB_887807
NMDAR2D Polyclonal Antibody	Thermo Fisher Scientific	Cat# PA5-87624; RRID: AB_2804299
/GLUT2 antibody	Synaptic Systems	Cat# 135403; RRID: AB_887883
Anti-PSD95 antibody	Abcam	Cat# ab18258; RRID: AB_444362
Rabbit anti-PGP9.5 Ab	Dako Deutschland GmbH	Cat# Z5116; RRID: AB_2622233
Anti-PGP9.5 antibody	Abcam	Cat# ab8189; RRID: AB_306343
GAPDH Antibody (6C5)	Santa Cruz Biotechnology Biotechnology	Cat# sc-32233; RRID: AB_627679
Ezh2 (D2C9) XP® Rabbit mAb	Cell Signaling Technology	Cat# 5246s; RRID: AB_10694683
Fri-Methyl-Histone H3 (Lys27) (C36B11) Rabbit mAb	Cell Signaling Technology	Cat# 9733s; RRID: AB_2616029
Acetyl-Histone H3 (Lys27) (D5E4) XP® Rabbit mAb	Cell Signaling Technology	Cat# 8173s; RRID: AB_10949503
E2F-1 Antibody	Cell Signaling Technology	Cat# 3742s; RRID: AB_2096936
Anti-Retinoblastoma (Rb)	BD Pharmingen™	Cat# 554136; RRID: AB_395259
cyclin D1 Antibody (A-12)	Santa Cruz Biotechnology	Cat# sc-8396; RRID: AB_627344
o16 (M-156)	Santa Cruz Biotechnology	Cat# sc-1207; RRID: AB_632106
DDK4 (DCS-35)	Santa Cruz Biotechnology	Cat# sc-23896; RRID: AB_627239
Phospho-Rb (Ser807/811) (D20B12)	Cell Signaling Technology	Cat# 8516S; RRID: AB_11178658
Phospho-Rb (Ser780) (D59B7)	Cell Signaling Technology	Cat# 8180S; RRID: AB_10950972
Anti-β Tubulin Antibody (D-10)	Santa Cruz Biotechnology	Cat# sc-5274; RRID: AB_2288090
Rabbit Anti-CAMKIV Polyclonal Antibody	Abcam	Cat# ab3557; RRID: AB_303904
Phospho-CREB (Ser133) (87G3) Rabbit mAb	Cell Signaling Technology	Cat# 9198S; RRID: AB_2561044
CREB (48H2) Rabbit mAb	Cell Signaling Technology	Cat# 9197S; RRID: AB_331277
Rabbit Anti-TGF alpha Polyclonal Antibody	Thermo Fisher Scientific	Cat# BS-0066R; RRID: AB_10856780
EGF Receptor (D38B1) XP Rabbit mAb	Cell Signaling Technology	Cat# 4267s; RRID: AB_2246311
EGFR antibody [EP38Y]	Abcam	Cat# ab52894; RRID: AB_869579
Anti-Substance P Monoclonal Antibody	Abcam	Cat# ab14184; RRID: AB_300971
CGRP (D5R8F) Rabbit mAb	Cell Signaling Technology	Cat# 14959s; RRID: AB_2798662
/anilloid R1/TRPV1 Antibody	Novus Biologicals	Cat# NB100-1617; RRID: AB_10002124
Cytokeratin Pan Antibody Cocktail	Thermo Fisher Scientific	Cat# MA5-13203; RRID: AB_10942225
Cytokeratin 19 antibody	DSHB	Cat# TROMA-III; RRID:AB_2133570
Caspase 9 (Cleaved Asp353) Polyclonal Antibody	Thermo Fisher Scientific	Cat# PA5-105271; RRID: AB_2816721
Beta Actin antibody	Santa Cruz Biotechnology	Cat# sc-69879; RRID: AB_1119529
Synaptobrevin1 antibody	Synaptic Systems	Cat# 104 004; RRID: AB_2619755
/GLUT2 antibody	Synaptic Systems	Cat# 135 409; RRID: AB_2943526
Anti-TRPV1 (VR1) Antibody	Alomone Labs	Cat# ACC-030; RRID: AB_2313819
SLC7A11 Polyclonal Antibody	Thermo Fisher Scientific	Cat# PA1-16893; RRID: AB_2286208
Anti-NMDAR1 antibody [N308/48]	Abcam	Cat# ab134308; RRID: AB_2818983
Biological samples		
Pancreatic ductal adenocarcinoma samples	Department of Surgery at the Technical University of Munich, Germany	N/A

(Continued on next page)



Continued				
REAGENT or RESOURCE	SOURCE	IDENTIFIER		
Human celiac ganglia specimens	Department of Surgery at the Technical University of Munich, Germany	N/A		
Chemicals, peptides, and recombinant proteins				
Albumin Fraction V (BSA)	Carl Roth GmbH	Cat# T844.3		
Ammonium persulfate (APS)	Carl Roth GmbH	Cat# 9592.1		
Citric acid (Monohydrate)	Carl Roth GmbH	Cat# 3958.4		
3-27 Supplement (50x)	Gibco	Cat# 1116531		
BCA protein assay	Thermo Fisher Scientific	Cat# 23225		
ECL Plus Western Blotting substrate	Thermo Fisher Scientific	Cat# 32132		
Extracellular matrix (ECM) gel	Sigma-Aldrich Chemie GmbH	Cat# E1270		
Glycine	Carl Roth GmbH	Cat# 3908.3		
Collagenase type II	Worthington Biochemicals	Cat# LS004176		
EGF	Invitrogen	Cat# 17005042		
Dulbecco's Phosphate Buffered Saline	Sigma	Cat# D8537		
Fetal Bovine Serum	Sigma-Aldrich Chemie GmbH	Cat# F7524		
GluN2D NMDAR antagonist UBP145	Hellobio	Cat# HB4717		
HEPES solution	Sigma-Aldrich Chemie GmbH	Cat# H0887		
Fluorescence Mounting Medium	Dako Deutschland GmbH	Cat# S3023		
(APA SYBR® FAST Kit for LightCycler® 480	Sigma (Rothe)	Cat# KK4611		
Hank's BSS	PAA	Cat# H15-010		
Methanol	Carl Roth GmbH	Cat# 4627.5		
luclease-Free water	Invitrogen	Cat# 2004098		
3mm round coverslip	Neolab	Cat# 1-6284		
nydrogen peroxide 30%	Carl Roth GmbH	Cat# 9681.1		
-Glutamine solution	Sigma-Aldrich Chemie GmbH	Cat# G7513		
Aatrigel	CORNING	Cat# 356231		
Ethanol absolute	Merck KGaA	Cat# 64-17-5		
DAPI	Abcam	Cat# ab228549		
-glutamate	Abcam	Cat# ab120049		
Vatriumchlorid (NaCl)	Carl Roth GmbH	Cat# 3957.2		
Milk	Carl Roth GmbH	Cat# T145.3		
		Cat# C0775		
Crystal Violet	Sigma-Aldrich	Cat# 50062Z		
Normal goat serum	Life technologies			
Veurobasal medium	Gibco	Cat# 21103		
(PL Biotinylated antibody goat anti-mouse IgG	Sera Care	Cat# 10247762		
Minimum Essential medium Eagle (MEM) media	Sigma-Aldrich Chemie GmbH	Cat# M2279		
Mitomycin C	Sigma-Aldrich	Cat# M4287		
RIPA buffer	Sigma-Aldrich Chemie GmbH	Cat# R0278		
KPL Streptavidin/Phosphatase Reagent	Sera Care	Cat# 140375		
Penicillin-Streptomycin	Sigma-Aldrich Chemie GmbH	Cat# P0781		
PBS Dulbecco	Biochrom GmbH	Cat# L182-50		
Roticlear	Carl Roth GmbH	Cat# A538.1		
Rotiphorese Gel 30	Carl Roth GmbH	Cat# 3029.1		
phosphatase inhibitor	Sigma-Aldrich Chemie GmbH	Cat# 4906837001		
protease inhibitor	Sigma-Aldrich Chemie GmbH	Cat# 4693159001		
SDS, ultra-pure	Carl Roth GmbH	Cat# 2326.2		
DS sample buffer (4X)	Invitrogen	Cat# 2197595		
Sample Reducing Agent (10X)	Invitrogen	Cat# 2032941		
Oulbecco's Modified Eagle's Medium (500 ml)	Sigma	Cat# D5671-500ML		

(Continued on next page)



Continued		
REAGENT or RESOURCE	SOURCE	IDENTIFIER
Tris base		
TEMED	Sigma-Aldrich Chemie GmbH Carl Roth GmbH	Cat# T1503 Cat# 2367.3
	Thermo Fisher Scientific	Cat# 34577
Super Signal West Pico PLUS Chemiluminescent Substrate	Thermo Fisher Scientific	Gat# 345/7
Triton X 100	Carl Roth GmbH	Cat# 3051.2
Trypsin-EDTA solution	Sigma-Aldrich Chemie GmbH	Cat# T3924
Tris-HCl	Sigma-Aldrich Chemie GmbH	Cat# T3253
ε-aminocaproic acid	Sigma-Aldrich Chemie GmbH	Cat# 7260
Opti-MEM™ I Reduced Serum Medium	Thermo Fisher Scientific	Cat# 31985070
Tween 20	Carl Roth GmbH	Cat# 9127.2
VectaMount Permanent Mounting Medium	Vector	Cat# H-5000
Lipofectamine™ RNAiMAX Transfection Reagent	Thermo Fisher Scientific	Cat# 13778075
Critical commercial assays		
Glutamate assay kit	Abcam	Cat# ab83389
Pierce™ Magnetic ChIP Kit	Thermo Fisher Scientific	Cat# 26157
RNeasy plus mini Kit (250)	QIAGEN	Cat# 74136
High-Capacity cDNA Reverse Transcription Kit	Thermo Fisher Scientific	Cat# 4368814
RQ1 RNase-Free DNase	Promega	Cat# M6101
HistoMark RED Phosphatase Substrate Kit	Insight Biotechnology	Cat# 5510-0036
Substance P Assay Kit	R&D Systems	Cat# KGE007
Maus CGRP Kit Elisa	Antibodies.com	Cat# A76318
TRPV1 ELISA Kit	antikoerper-online.de	Cat# ABIN1503996
NE-PER™ Nuclear and Cytoplasmic Extraction Reagents	Thermo Fisher Scientific	Cat# 78835
Deposited data		
The TCGA pan-cancer and pancreatic adenocarcinoma (PAAD) datasets	Genomic Data Commons (GDC) portal	https://portal.gdc.cancer.gov/
scRNA-seq dataset	Hwang et al. ³³	GSE202051
scRNA-seq dataset	Cui et al. ³⁴	phs002371.v1.p1
Raw sequencing data	This paper	GSE291933
Experimental models: Cell lines		
SU.86.86	ATCC	CRL-1837™; RRID: CVCL_3881
T3M4	Provided by Dr. Metzgar from Duke University Medical Center, Durham, North Carolina	N/A
PANC-1	ATCC	CRL-1469™; RRID: CVCL_0480
Capan-1	ATCC	HTB-79™; RRID: CVCL 0237
Human neuroprogenitor cell line SPC-01	Provided by Dr. Nataliya Romanyuk from Department of Neuroregeneration, Institute of Experimental Medicine, CAS, Vestec, Czechia	N/A
Experimental models: Organisms/strains		
B6.129X1-Trpv1 ^{tm1Jul/J} mice	Jackson Laboratory	Stock No: 003770; RRID:IMSR_JAX:003770
C57BL/6N wild-type	Charles River Laboratory	RRID:IMSR_CRL:27
Oligonucleotides	,	-
EZH2 siRNA (human))	siTOOLs	Cat# #2146
E2F1 siRNA (human)	siTOOLs	Cat# #1869
GRIN2D siRNA (human)	siTOOLs	Cat# #2906
CaMK IV siRNA (human)	siTOOLs	Cat# #0814
mGrin2d-Intron2-gRNA:	This study	Syntego Syntego
TGGGGGTTCTGGCAACTAAG	,	

(Continued on next page)



Continued		
REAGENT or RESOURCE	SOURCE	IDENTIFIER
mGrin2d-Intron3-gRNA: TATGACTTTCCATAACACGT	This study	Custom-synthesized by Syntego
Mouse Ezh2 SiPOOL 5 pool	siTOOLs	Cat# 14056
Recombinant DNA		
Mouse Grin2d shRNA in pLKO.1 vector	Sigma-Aldrich	TRCN0000100210, Gen-ID 14814
hGRIN2D-GFP expression plasmid	OriGene	RG224610
mSlc17a6-RFP expression plasmid	OriGene	CW310145
pT3EF1a-TGFA overexpression plasmid	This study (based on pCMV6-AC-GFP-TGFA)	N/A
Software and algorithms		
ImageJ	https://imagej.net/ij/	N/A
GraphPad Prism (version 9.2.0 or higher)	GraphPad Software Inc.	N/A
FlowJo (version 10.8.0)	FloJo, LLC	N/A
Amira Version 2019.4;	Thermo Fisher Scientific	N/A
Affinity Photo 2 (Version 2)	Serif Europe https://affinity.serif.com	N/A
LiveAquisition	Used for calcium imaging; contact vendor, FEI, Munich	N/A
ggplot2 v3.3.3	Wickham et al. ⁶⁶	https://ggplot2.tidyverse.org/
Scanpy v1.11	Wolf et al. ⁶⁷	https://scanpy.readthedocs.io/en/stable/
OfflineAnalysis	Used for calcium imaging; contact vendor, FEI, Munich	N/A

EXPERIMENTAL MODEL AND STUDY PARTICIPANT DETAILS

Patient samples

Patient samples were collected from 20 PDAC patients who underwent resection at the Department of Surgery at the Technical University of Munich, Germany. Tumor tissues and celiac ganglia were obtained and processed accordingly. Tumor tissues were fixed in 4% paraformaldehyde in PBS overnight and subsequently embedded in paraffin. Thin slices with a thickness of 2.5 μm were prepared for immunostaining analyses. All human specimens (resected PDAC tissues) included in this study were collected with informed consent and approved by the Ethics Committee of the Technical University of Munich (nr: 2016-550-S-SR).

Cell lines and cell culture

The human PDAC cell line SU.86.86, PANC-1 and Capan-1 were procured from the American Type Culture Collection. The T3M4 cell line was generously provided by Dr. Metzgar from Duke University Medical Center, Durham, North Carolina.

Human neuroprogenitor cell line SPCs-01 (SPCs) was generated and provided by Dr. Romanyuk.

Murine primary pancreatic cancer cell lines were derived from fresh murine cancer cells selected via serial passage selection. Murine cell lines were utilized as follows: KPC primary cell line-Ptf1a^{+/Cre};Kras^{+/LSL-G12D};Trp53^{+/fl}; KPC-Pdx1CRE^{+/Cre}; Kras^{+/LSL-G12D};Trp53^{R172H}; TPAC-Ela1-TGFa;Ptf1a^{+/Cre};Trp53^{fl/fl}:p65^{fl/fl}. Murine dorsal root ganglia (DRGs) for primary DRG cultures were isolated as described previously. On brief, DRGs dissected from 3- to 10-day-old C67BL/6N mice were digested with Collagenase and cultured in neurobasal medium supplied with 0.5 mM L-glutamine, 1% penicillin/streptomycin, 2% B27 (Gibco), and 10% FCS. Conditioned medium (CM) from DRG cultures was prepared by incubating confluent DRG cultures with serum-free medium for 24 hours, followed by storage at -80°C.

For experiments involving L-glutamate and DRG CM treatments, 3x10⁵ PDAC cells were seeded into a 6-well plate. Prior to treatment, cells were starved of glutamine and serum overnight. Subsequently, cells were subjected to stimulation with L-glutamate or DRG CM for a duration of 48 hours before being harvested for further analysis.

Mouse experiments

All animal experiments were performed following the governmentally approved animal experiment protocols. 4-5-week-old adult B6.129X1-*Trpv1*^{tm1Jul/J} (*Trpv1* KO, Strain #:003770) mice were purchased from The Jackson Laboratory. Six-week-old C57BL/6N wild-type (WT) and *Trpv1* knockout (KO) mice were used for orthotopic implantation studies at the ZPF animal facility of the Technical University of Munich.

For orthotopic implantations, KPC-Pdx1CRE cells were used. Briefly, 1×10^6 Grin2d-gene-edited cells and their control cells were injected in 50μ l DMEM into the pancreas of anesthetized C57BL/6N mice using 26-gauge needles. The tumor size was assessed by ultrasonography. Mice from the cohort where overall survival was analyzed were sacrificed after the tumors reached a size of 1 cm. In

Cancer CellArticle



the tissue-collection cohort, mice were sacrificed on day 55 post-implantation and used for RNA sequencing. All animal experiments were approved by the Ethics Committee of the Technical University of Munich and the Governmental Commission for Animal Protection of the Government of Upper Bavaria (Regierung von Oberbayern, no. 55.2-2532-Vet-02-17-98 and Vet-02-23-110).

METHOD DETAILS

Migration assay with time-lapse microscopy

Time-lapse microscopy was performed using *GRIN2D*^{-/-} and *GRIN2D*^{-/-} KPC-Pdx1CRE cells, as described previously.^{31,61-63} Briefly, 1x10⁵ cancer cells and 5x10³ DRG cells were suspended in the extracellular matrix (ECM) droplets (Sigma-Aldrich, E1270) and positioned 5 mm apart. The ECM droplets were interconnected via ECM gel bridges, and incubated in DRG culture medium for 48 hours. Time-lapse video microscopy (Zeiss AxioObserver Z1) was employed to capture migration dynamics over a 48-hour period. Parameters such as the forward migration index (FMI), Euclidean distance, and velocity of cancer cells migrating toward DRGs were quantified to assess migratory behavior, following established methodologies.^{31,61-63}

Ablation of sensory fibers for the tumor growth following KPC-Pdx1CRE cell implantation

Sensory neurons were ablated using i.p. capsaicin treatment at postnatal day 2 (P2). Briefly, 20 μ L 50 mg/kg of capsaicin (i.p.) in a solution of absolute ethanol/Tween-80/isotonic saline (1:1:8) was administered. Then, KPC-Pdx1CRE $Grin2d^{-/-}$ cells were orthotopically implanted into the pancreas of six-week-od C57BL/6N mice. At the age of 99 days, capsaicin-treated mice were euthanized, and tissues were collected for histological analyses.

Cell treatments, wound healing assay, colony formation assay, MTT assay, and cell invasion assay

Concentration screening for L-glutamate or the GRIN2D antagonist UBP145 involved exposing cells to L-glutamate at concentrations ranging from 0 to 10.0 μ M or 0.2 μ M glycine, ⁶⁴ or to UBP145 at concentrations ranging from 0 to 1000 μ M for 48 hours.

For GRIN2D blocking experiments using UBP145, cells were treated with 10 μ M UBP145 for 30 minutes after removal of the silicone culture inserts.

For wound healing assays, cells pretreated with starvation were seeded into two-well silicone culture inserts (Ibidi, 80241). Prior to insert removal, cells were treated with mitomycin C, and fresh medium containing 0.5 µM L-glutamate or DRG conditioned medium (CM) containing 0.5 µM L-glutamate was applied. Images were captured using a microscope connected to an AxioCam MRm camera after 24 hours.

For colony formation assays, 500 cells with Grin2d depletion were seeded in six-well plates and cultured for two weeks.

MTT assays were conducted in triplicates using 96-well plates. Cells (5000 cells/well) were seeded and grown for 24 hours after overnight starvation of glutamine and serum. Cell viability was assessed using dissolved 3-(4,5-dimethyl-2-thiazolyl)-2,5-diphenyl-2H-tetrazolium bromide (MTT, Sigma-Aldrich) dye with dimethyl sulfoxide (DMSO).

Cell invasion assays were performed in 24-well plate transwell units with an 8 μ M-pore-size membrane chamber (Corning, NY) and glutamine-/serum-free medium. Starvation-pretreated cancer cells (5x10⁴) were seeded in upper chambers precoated with 60 μ I Matrigel (BD Biosciences) for at least 4 hours. The lower chambers were filled with medium containing 0.5 μ M L-glutamate or DRG CM. Invading cells were fixed with ice-cold methanol, stained with crystal violet, and dissolved in glacial acetic acid.

Immunocytochemical (ICC), immunohistochemical (IHC), and immunofluorescent (IF) staining

For immunocytochemical (ICC) staining, cells fixed with 4% paraformaldehyde (PFA) were placed on coverslips, permeabilized, blocked, and then incubated with respective primary antibodies overnight at 4°C. Subsequently, cells were incubated with secondary antibodies conjugated with Alexa Fluor 488/594/647/750 and DAPI for 1 hour at room temperature, and coverslips were mounted on slides. Images were captured using a Keyence microscope.

For immunohistochemical (IHC) and immunofluorescent (IF) stainings, formalin-fixed paraffin-embedded (FFPE) slides were deparaffinized and rehydrated. Antigen retrieval was performed, followed by treatment with 3% hydrogen peroxide (for IHC) and protein blocking. Slides were then incubated with primary and secondary antibodies of interest. For double IHC staining, the DAB substrate staining kit was utilized either with the HistoMark RED Phosphatase Substrate or KPL Streptavidin/Phosphatase Reagent. Quantification was carried out using ImageJ and QuPath Software. To estimate the number of neurons in T8–T12 DRGs, DRG tissues were sectioned at 14 μ m and analyzed via systematic random sampling (every fifth section) and counting of neuronal nuclei.

Gene editing

For generation of the knockdowns, siRNAs for human genes *EZH2*, *E2F1*, *GRIN2D*, and *CaMK IV* siRNA (2146, 1869, 2906, and 814, respectively, from siTOOLs) and shRNA for murine *Grin2d* [TRCN0000100210 (GCACAGGTATTTCATGAACAT), Gen-ID 14814, Merck] were used. For labeling of cancer and neural cells, plasmids with h*GRIN2D*-GFP tag, and m*Slc17a6*-RFP tag (RG224610 and CW310145, respectively, from OriGene) were utilized. For delivery of gene-editing tools into the target cells, Lipofectamine™ RNAiMAX Transfection Reagent (Thermo Fisher) and Lipofectamine™ 3000 (L3000008, Thermo Fisher) were used. Puromycin was used for stable selection in shRNA transfections.

For Grin2d gene knockout by CRISPR-Cas9 tools, cells were cultured in 48-well plates until 90% confluency. Ribonucleofection was carried out using specific gRNAs (Syntego 1.5 nm), Cas9 protein (1 μ M), and X-tremeGENE 360 transfection reagent (Roche).





Following ribonucleofection, cells were incubated for 48 hours at 37°C. Subsequently, single cells were cultured in 96-well plates for selection of the single clones. Editing efficiency was assessed by PCR on genomic DNA and by western blot analysis.

For overexpression, human TGFA cDNA, amplified from pCMV6-AC-GFP-TGFA, was cloned into the transposon vector pT3EF1a (a kind gift from Dr. Xin Chen's lab) using Gibson assembly and verified by sequencing. Cancer cells were transduced via electroporation with the TGFA transposon plasmid and the SB13 transposase plasmid. Successful integration was confirmed by sequencing.

Real-time quantitative PCR (RT-qPCR) and chromatin immunoprecipitation (ChIP)-PCR assay

Total RNA was extracted from human and murine tissues and cells using the RNeasy Plus Mini Kit (Qiagen), followed by cDNA synthesis using the RQ1 RNase-Free DNase kit (Promega) and the High-Capacity cDNA Reverse Transcription Kit (Thermo Fisher). PCR amplification of cDNA was performed using the KAPA SYBR® FAST Kit (Sigma, Roth) in triplicate on a LightCycler 480 machine.

For chromatin immunoprecipitation (ChIP)-PCR assays, the Pierce Magnetic ChIP Kit (Thermo Fisher) was employed according to the manufacturer's instructions. Immunoprecipitation was carried out using Magnetic Beads conjugated with target-specific antibodies (anti-EZH2 and anti-E2F1) of ChIP-grade quality, while anti-IgG and anti-RNA polymerase II antibodies were used as negative and positive controls, respectively. Primer sequences used in the assays are provided in Table S1.

Western blot and ELISA

For Western blot analysis, cells were lysed in RIPA buffer (Sigma, R0278) supplemented with phosphatase inhibitor (PhosSTOP) and protease inhibitor (EDTA-free). After lysing, cells were sonicated on ice and the protein concentrations were determined using a BCA protein assay kit.

Nuclear and cytoplasmic protein extraction was performed using the NE-PER Nuclear and Cytoplasmic Extraction Reagents (78835, Thermo Fisher) following the manufacturer's protocol. The proteins were adjusted to a uniform concentration of 1 μg/μl using loading dye, boiled for 5 minutes at 95°C, and cooled on ice. Subsequently, 20 μg of proteins were separated by SDS-PAGE and transferred onto nitrocellulose membranes. After blocking, the membranes were probed with primary antibodies including anti-GRIN2D (PA5-101608 and PA5-87624, Thermo Fisher), anti-GRIN1 (PA3-102, Thermo Fisher), anti-synaptobrevin-1 (104002, Synaptic Systems), anti-vGlut-2 (135403, Synaptic Systems), anti-PSD95 (ab18258, Abcam), anti-GAPDH (SC-32233, Santa Cruz Biotechnology), anti-EZH2 (5246s, Cell Signaling), anti-H3K27me3 (9733s, Cell Signaling), anti-H3K27ac (8173s, Cell Signaling), anti-E2F1 (05-379, Upstate), anti-Retinoblastoma (Rb) (554136, BD Pharmingen[™]), anti-cyclin D1 (sc-8396, Santa Cruz), anti-CDKN2A (sc-1207, Santa Cruz), anti-CDK4 (sc-23896, Santa Cruz), anti-Phospho-Rb (Ser807) (8516S, Cell Signaling), anti-phospho-Rb (Ser780) (8180S, Cell Signaling), anti-Beta-Tubulin (sc-5274, Santa Cruz Biotechnology), anti-CaMK IV (ab3557, Abcam), anti-EGFR (ab52894, Abcam), anti-phospho-CREB (Ser133) (9198T, Cell Signaling), anti-SLC7A11 (PA1-16893, Thermo Fisher), anti-GLAST (PA5-72895, Thermo Fisher), and anti-CREB (9197S, Cell Signaling). The density of the protein bands was quantified using ImageJ software after incubation with secondary antibodies and membrane visualization.

For ELISA protein measurements, the protein, and glutamate of cells, their supernatants, and 10 mg of tumor tissue samples including the pancreas, blood, and T8-T12 DRGs of implanted mice were determined using corresponding kits: Glutamate assay kit (ab83389, Abcam), CGRP Kit Elisa (A76318, Antibodies), TRPV1 ELISA Kit (ABIN1503996, antikoerper-online.de), Mouse TGF alpha ELISA Kit (A3364, antibodies.com) and Substance P Parameter Assay Kit (KGE007, R&D Systems).

Inhibitors and recombinant proteins

For the assessments of neuron growth originating from dorsal root ganglia (DRG) and sensory neuron ablation, recombinant human TGF-alpha (rhTGF-alpha; R&D Systems, 239-A-100) or capsaicin (R&D Systems, 0462/100) were utilized to treat the DRG cultures.

Bioinformatic analysis

The gene signature of 23 glutamatergic receptor, including the four types described below, was defined through its core components. Gene levels were normalized using the housekeeping gene (HKG), and the geometric mean of the ranks (rank product) of the per-sample gene expression was calculated.

NMDAR: GRIN1, GRIN2A, GRIN2B, GRIN2C, GRIN2D, DLGAP1.

AMPAR: GRIA1, GRIA2, GRIA3, GRIA4.

Kainate: GRIK1, GRIK2, GRIK3, GRIK4, GRIK5.

Metabotropic: GRM1, GRM2, GRM3, GRM4, GRM5, GRM6, GRM7, GRM8.

The distributional levels of glutamate receptors in patient PDAC and paired ganglia were analyzed. Differential gene expression analysis of unpaired samples was performed using UCSC XENA's unified TCGA and GTEx RNA-seq data (TPM format) processed by the Toil pipeline, ⁶⁵ including 171 human normal pancreas and 179 human PDAC tissues. RNA-seq data from TCGA PDAC project level 3 in HTSeq-FPKM (Fragments Per Kilobase per Million) format were used for the correlation analysis of potentially related molecules. The RNA-seq data in FPKM format were converted into TPM, and log2 conversion was performed to compare the expression levels. The Mann-Whitney U tests (Wilcoxon rank-sum tests) and Spearman's correlation analysis were performed using the ggplot2 (version 3.3.3) R package. ⁶⁶

Single-cell RNA sequencing (scRNA-seq) datasets from two independent PDAC studies (GSE202051 and dbGaP Study phs002371.v1.p1)^{33,34} were analyzed using Scanpy (v1.11) in Python.⁶⁷ Raw gene expression count matrices were imported, and

Cancer CellArticle



pre-processing involved filtering for high-quality cells, followed by normalization and dimensionality reduction. Cell populations were annotated using canonical markers for malignant epithelial cells, fibroblasts, endothelial cells, and immune cell subsets.

Scanning & transmission electron microscopy

For cancer-neurons pseudo-synapse of co-cultures by using a scanning electron microscope (SEM), SU.86.86-Neurons co-cultures for FIB/SEM were cultivated on glass slides, fixed with 2.5% glutaraldehyde (Electron microscopy sciences, 16220), post-stained with 2% osmium tetroxide, dehydrated, and flat-embedded as described previously. ⁶⁸ FIB/SEM-tomography was performed with an Auriga 40 crossbeam station, involved milling with an ion beam for 2 nm slices. ⁶⁹ Voxel size ranged from 10 to 15 nm, and images were captured using specific settings (1.5 kV acceleration voltage, 500 V ESB-grid setting, and 30 µm aperture), resulting in 2048 x 1536 pixel-images, while ultrathin sections were examined and documented using a LEO912AB or a JEOL F200 transmission electron microscope.

For the 3D reconstruction of the FIB-SEM tomogram, Amira (version 2019.4) was utilized for segmentation. A label field was created within the tomogram, and the segmentation was performed on it. Distortions from the focused ion beam (FIB) were addressed using Affinity Photo 2, and misalignments were corrected using the StackReg and TurboReg plugins in ImageJ. Images were loaded into Amira, and the correct voxel size was set to $14 \times 14 \times 20$ nm for accurate segmentation. Magic wand-based segmentation was repeated every five images, and the interpolation function filled in the gaps between the segmented images. Membrane and neuron segmentation were achieved through a manual approach using a brush, and the label field was resampled to a consistent dimension of $2 \times 2 \times 2$ after assigning different materials to the segmentation objects, ultimately generating 3D reconstruction.

For transmission electron microscopy (TEM), semithin and ultrathin sections from PDAC tumor specimens were prepared as previously published. 70,71 Fresh PDAC tumor tissues underwent resection and were immersed in 2% glutaraldehyde in 0.1M cacodylate buffer at pH 7.5 for fixation. Post-fixation was performed with 1% osmium tetroxide, followed by dehydration in an ethanol series and infiltration with epoxy embedding medium. Semithin (1.5 μ m) and ultrathin sections (60 nm) were cut, mounted, and stained accordingly. Evaluations of semithin sections were conducted using an AxioLab microscope, while ultrathin sections were examined and documented using a LEO 912AB transmission electron microscope.

Calcium signal (Ca-signal) imaging

To assess calcium signals in response to drug application, ratiometric calcium imaging was performed. 72 Briefly, a 1 mM Fura-2 AM stock was prepared by adding 50 µl DMSO to a 50 µg vial of crystalized Fura-2 AM (Invitrogen, F1221), and cells on cover slides were stained with this solution (2 µl of the 1 mM Fura-2 AM + 2 ml of 37°C co-culture medium) for 45 minutes at 37°C with 5% CO2 and 95% O2 in a dark incubator. For Ca-signal recording, the cover slides were put in a recording chamber and continuously perfused with artificial cerebrospinal fluid containing 125 mM NaCl, 2.5 mM KCl, 25 mM NaHCO3, 2 mM CaCl2, 1 mM MgCl2, 25 mM d-glucose, 1.2 mM NaH2PO4 and 10 µm d-serine, which was bubbled with carbogen (95% O2/5% CO2). Using a xenon lamp (Till Photonics, Polychrome V), two sequential light pulses, one at 350 for 120ms followed by 380 for 120ms, were delivered via a 63x objective (Zeiss 440067, Achroplan, 63x/0,09 W) to the cells and the emission of the Fura-2 stained cells was measured using the LiveAquisition program (FEI, Munich), Fura-2 signal intensity at 350 nm is dependent on calcium concentration, while the one measured at 380 nm is independent. Fura-2 dual-wavelength excitation allows therefore quantitative measurement of Ca-signals, independently from the dye concentration by measuring the ratio of 350/380 in each acquisition cycle (around 120ms). Ca-signals were elicited via a puffing system (PDES-02DX, npi, Tamm, Germany). The puffing system allowed a very precise application of the neurotransmitter glutamate (0,1 mM, 0,3 mM, 1 mM or 3 mM) to only one single cell for a very specific period (100 ms, 500 ms or 1000 ms) via a borosilicate glass pipet (BF150-117-10, Sutter, Chicago, USA) pulled to an open tip resistance of 4 MΩ on a micropipette puller (Flaming/Brown Micropipette Puller Model P-1000, Sutter, Chicago, USA) and positioned directly next to the cell of interest. After recording of a short baseline (about 20-25s), the puffing of glutamate was performed and the cells response was measured for about 180-200s. Offline analysis (OfflineAnalysis, FEI, Munich) was performed on the whole image by drawing regions of interest around the pancreatic cancer cells, that show a good signal-to-noise ratio. For the Ca-imaging recordings, we distinguished between DRG and cancer cells based on their very distinct morphologies. This allowed us to precisely mark our regions-of-interest on individual cancer cells, ensuring no signal-interference from the sourrounding DRG cells. One additional ROI was drawn in an area devoid of signal as a control region and later eliminated from the analysis. The program automatically performs ratio calculation and background correction. The data was exported as an Excel sheet. For further analysis, the data was normalized to the baseline and the peak amplitude and AUC of the signal was measured.

Von Frey test

Mechanical pain sensitivity in the upper abdomen was assessed by counting withdrawal responses to Von Frey filament stimulation. Mice were placed on a raised wire mesh under a clear plastic box. Filaments were applied perpendicularly to the left upper abdominal region until bending, with each filament delivered 10 times (1–2 sec each, 5–10 sec intervals) in ascending order of force. Responses were scored as 0 (no response), 1 (mild response), or 2 (intense response), yielding a total score of 0–20 per filament. Seven filaments with evaluator sizes: 1.65 (target force: 0.08 mN), 2.36 (0.2 mN), 2.44 (0.4 mN), 2.83 (0.7 mN), 3.22 (1.6 mN), 3.61 (3.9 mN) and 3.84 (5.9 mN) were used to define the dynamic range. Data were analyzed via linear regression and expressed as $Y = a \times X - b$, where 'a' represents the response level and b/a indicates minimal sensitivity. 73





QUANTIFICATION AND STATISTICAL ANALYSIS

All statistical analyses were performed using GraphPad Prism (version 9.0), and graphical representations were generated using the same software. Data are presented as mean ± SEM, unless otherwise specified in the figure legends. For comparisons between two groups, including CWA, invasion assays, RT-qPCR, Western blot quantifications, and ELISA measurements (Figures 1E–1L, S2F–S2K, S3E–S3H, S3J–S3K, 3A, 3C–3F, S4D, S4F–S4L, 4A, 4E–4G, S5A, S5C–S5I, S6B, S6C, S6F, S6H, 5B, 5G–5I, S7B, S7H, 6B, 6C, 6I, 6J, S9A–S9C, S9F, and S9G), statistical significance was assessed using unpaired two-tailed Student's t-tests. Imaging-based quantifications, including immunostaining analysis, axonal count, and neuron counts (Figures 2A, 2B, 4H, 4I, S5B, 5C–5E, 6D–6F, S10C, S10E, and S10G), were also analyzed using unpaired two-tailed Student's t-tests. Survival differences across the groups (Figures 4D and S9M) were tested using the Log-rank (Mantel-Cox) test and visualized with Kaplan-Meier curves. Spearman's rank correlation test was used for correlation analyses (Figures S1E, S4A, and S4B). For analyses of TCGA dataset-derived expression profiles (Figures S1A–S1D), the Wilcoxon rank-sum test was applied. P-values < 0.05 were considered statistically significant. Statistical significance is denoted as follows: *p < 0.05, **p < 0.01, ****p < 0.001, *****p < 0.0001. All experimental quantifications were performed from at least three independent biological replicates unless otherwise specified in the figure legends.